Volume 2 Issue 2 August 2026

fast DART

DATA, ANALYSIS, REVIEWS, TECHNIQUES E-JOURNAL

Table of Contents

August 2026; Volume 2, Issue 2

Review Articles

UBE3A Isoform Biology in Health and Disease
Heather Born
Pages 1-12

Biotechniques Articles

Delivery of Recombinant Adeno-Associated Virus into the Rodent Brain
Marselina Levis Rabi, Natalia Hurst-Calle, Jonathan Willman, Matthew Willman, Casey Cook, Aurelie Joly-Amado and Kevin R. Nash
Pages 13-23

Standardized Electrophysiological Approaches for CA1 Field Recordings: Insights into the AS Mouse Model
Melinda M Peters, Joseph E. Pick and Edwin J Weeber
Pages 24-37

Editor-in-Chief ……. Edwin Weeber
Production Director …….. Meghan Edberg
Digital Director …….Amy Schamp
Creative Director …….……..Jena Berndt
Copy Editor……Kelly Knee

fast DART
DATA, ANALYSIS, REVIEWS, TECHNIQUES E-JOURNAL

Review

UBE3A Isoform Biology in Health and Disease

Heather Born[1]

[1] GEMMA Biotherapeutics, Philadelphia, PA, USA

Article History
Submitted: September 18, 2025 Accepted: October 24, 2025 Published: November 1, 2025

Abstract

Ubiquitin protein ligase E3A (UBE3A) is expressed in neurons throughout the brain and is critical for normal neuronal morphology and synaptic function. Altered UBE3A expression is implicated in several neurological disorders, most notably Angelman syndrome (AS), a rare genetic, non-degenerative, neurodevelopmental disorder that results from disruption of the maternal allele of *UBE3A* due to deletion, mutation, uniparental disomy, or imprinting center defect and leads to loss of neuronal UBE3A protein expression. Multiple isoforms of UBE3A are generated from the human gene sequence, and closely conserved mouse homologs show high sequence identity. Recent findings from the past few years using animal and cellular models, as well as insights from clinical studies in individuals with AS, have been instrumental for identifying isoform-dependent differences in expression, subcellular localization, structure, and contributions to both normal neuronal function and AS-related phenotypes. In this review, the current knowledge on the isoform-specific roles of UBE3A in normal physiology and disease pathology are summarized. Importantly, increased understanding of isoform-specific research questions will be informative for guiding future development of therapeutic strategies.

Keywords: UBE3A, isoforms, Angelman syndrome, expression, subcellular localization, function, neuron, translational science, human, mouse, gene therapy, development.

Introduction

Ubiquitin protein ligase E3A (UBE3A, also known as E6-AP) is essential for normal neuronal function and synaptic plasticity. Multiple isoforms of UBE3A exist, and prevailing evidence indicates that they each play distinct biological roles. Disruption to the normal expression and function of UBE3A gives rise to neurogenetic disorders, most notably Angelman syndrome (AS), which results from loss of expression in neurons. There is a significant unmet medical need for Angelman syndrome as no disease-modifying treatment is currently available and severe symptoms leave individuals unable to live independently. Greater understanding of the biology of UBE3A isoforms may provide new insights on therapeutic strategies for Angelman syndrome. This review considers isoform-dependent differences in expression, subcellular localization, structure, and functional roles of UBE3A in normal physiology and disease.

UBE3A Isoform Expression

The *UBE3A* gene is located in the 15q11–q13 region of chromosome 15. The sequence for *UBE3A* has a coding region of ~2.7 kb long containing 10 exons that encode 852-875 amino acids. *UBE3A* contains multiple functional domains: the E6 protein binding

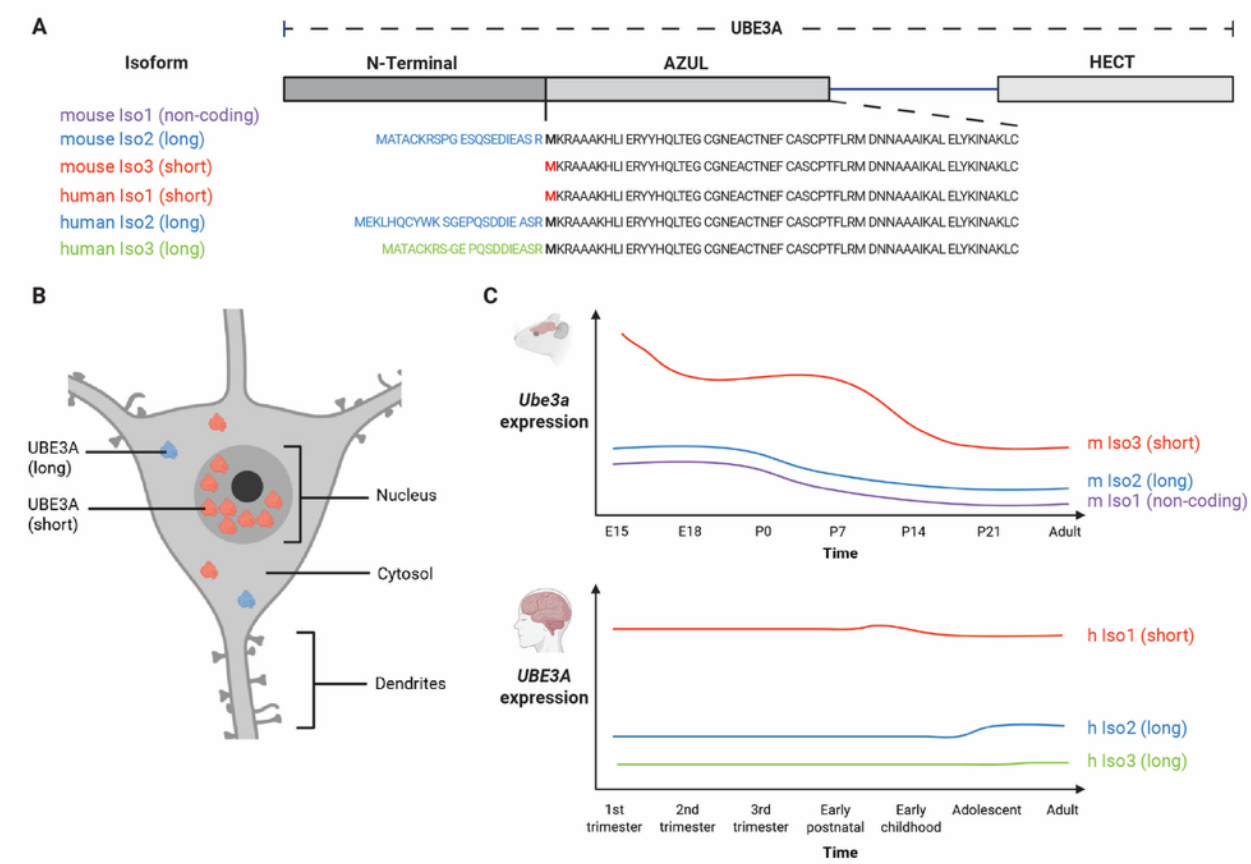

Figure 1.
(A) Schematic overview of the UBE3A amino acid sequence alignment for the mouse and human isoforms (adapted from Biagioni 2025 Fig 2 and Krzeski 2024 Fig 1).
(B) Subcellular localization and relative expression levels of UBE3A isoforms in the neuron.
(C) Expression pattern of *UBE3A* in brain in mice (adapted from Miao et al. 2013, Fig 2B) and humans (adapted from Judson et al. 2021 Fig 1C) throughout development.
Created with BioRender.

region, the amino-terminal zinc-binding domain of ubiquitin E3 ligase (AZUL), the HECT and RCC1-like domain 2 (HERC2), and the Homologous to E6-AP Carboxyl Terminus domain (HECT) (Huibregtse et al., 1993; Scheffner et al., 1994; Cooper et al., 2004; Kühnle et al., 2011; Avagliano Trezza et al., 2019). The loss of expression or function from the maternally inherited *UBE3A* gene causes Angelman syndrome, a rare neurogenetic, non-degenerative disorder with an incidence of 1:12,000-1:20,000) (Buiting et al., 1995; Fiumara et al., 2010; Mabb et al., 2011; Dagli et al., 2012). The most common causes for AS include maternal deletions within the chromosome 15q11-q13 region containing *UBE3A* (65-75%) or point mutations/variants within the *UBE3A* coding region (10-15%); less frequent causes include paternal uniparental disomy (UPD) (3-5%), an imprinting center defect (ICD) on the maternal allele (3-4%), and mosaicism (~1%) (Jana, 2012). Frequently, the genetic cause is a spontaneous *de novo* mutation involving the maternal *UBE3A* gene (Kishino et al., 1997; Matsuura et al., 1997). Inherited causes of AS are much rarer and due to a *UBE3A* point mutation or a subtype of ICD called submicroscopic deletion of the imprinting center, which results in bi-allelic neuronal silencing (Buiting et al., 1995; Van Buggenhout and Fryns, 2009; Dagli et al., 2012).

Early work identified 5 *UBE3A* mRNA transcripts generated by alternative splicing (Yamamoto et al., 1997) with more recent reports indicating there are ~50 mRNA transcripts (Yang and Huang, 2025). Three UBE3A protein isoforms (~100 kDa) have been identified in humans (isoform 1 [hUBE3A-iso1], isoform 2 [hUBE3A-iso2], and isoform 3 [hUBE3A-iso3]). These isoforms have complete sequence overlap with the exception of an extension at the N-terminal end in isoforms 2 and 3 due to translation from an independent start codon (Fig. 1A). hUBE3A-iso2 includes a 23-amino-acid N-terminal extension

and hUBE3A-iso3 includes a 20-amino-acid N-terminal extension. In line with the critical role of UBE3A in normal physiology and neurodevelopment, there are closely conserved murine homologs for the two human isoforms that make up the majority of expressed protein in neurons with 96% amino acid sequence identity to their respective orthologs (Zampeta et al., 2020). Extensive analysis to understand the different UBE3A isoforms has been completed using mouse-derived neuronal cell culture or using AS mouse models, such as the *Ube3a*$^{m-/p+}$ (Jiang et al., 1998) or *Ube3a*^{tm2Yelg} model (Wang et al., 2017); additional studies have used immortal cell lines, hESC-derived cells, AS donor hIPSC-derived neurons, and human post-mortem tissue.

Multiple *Ube3a* isoforms are found in mice as a result of alternative splicing or polyadenylation, including mouse *Ube3a* isoform 3 (*mUbe3a*-iso3), the short coding isoform that is homologous to *hUBE3A*-iso1 (91% sequence identity). Mouse *Ube3a* isoform 2 (*mUbe3a*-iso2) is the long coding isoform (an additional 21 amino acid N-terminal extension) and homologous to *hUBE3A*-iso3 (92% sequence identity) (Fig. 1A).

For a more detailed diagram of the *UBE3A* exonic structure and comparisons across different isoform transcripts, see Figs.1 and 2 in (Yamamoto et al., 1997) and Fig. 4 in (Zampeta et al., 2020). There is no known mouse homolog for *hUBE3A*-iso2, which arose later in evolution (Zampeta et al., 2020). An alternative polyadenylation signal results in a different 3' UTR and a truncated, inactive non-coding mouse *Ube3a* isoform 1 transcript with a coding-independent role in brain development that does not have a known human homolog (Valluy et al., 2015).

UBE3A is biallelically expressed in most tissues. In mature neurons, however, it is solely expressed from the maternal allele due to genomic imprinting and silencing of the paternal allele through RNA transcription of a long non-coding RNA (>600 kb) called the *UBE3A* antisense transcript (*UBE3A-ATS*) that initiates in the 15q11-q13 region of the paternal allele (Huibregtse et al., 1991; Mishra et al., 2009; Greer et al., 2010; Sato and Stryker, 2010; Kaphzan et al., 2012; Margolis et al., 2015). Paternal *UBE3A* is expressed in all other cell types, including peripheral tissues and glial cells in the nervous system, with a reduction of 50% or more found in UBE3A expression in peripheral tissues and cultured glial cells (Dindot et al., 2008; Gustin et al., 2010; Grier et al., 2015). UBE3A is expressed broadly throughout the brain with the strongest expression in neurons, both glutamatergic and GABAergic (Gustin et al., 2010; Judson et al., 2014; Burette et al., 2017; Burette et al., 2018). UBE3A protein expression in the brains of WT mice was found to be slightly higher in some regions, including the cortex, olfactory bulbs, and thalamus, than in other regions evaluated, such as the hippocampus, striatum, hypothalamus, cerebellum, and midbrain (Gustin et al., 2010). For an in-depth review of the spatial and temporal expression of UBE3A, see (Biagioni et al., 2024).

At the neuronal level, work from Dindot et al. using a *Ube3-YFP* reporter mouse demonstrated that UBE3A protein expression can be found at high levels in the nuclei of neurons as well as in the cell body, dendrites, in the growth cones of developing neurites, and both pre- and postsynaptic compartments (Dindot et al., 2008). Subcellular fractionation confirmed a broad distribution of UBE3A as well, with the highest level detected in the soluble protein pool and lower levels found in the membrane, postsynaptic density, and insoluble pools (Gustin et al., 2010). Analysis using high-resolution immunogold electron microscopy and confocal co-localization confirms that expression is unevenly distributed, with the highest intensity/density of staining found in small puncta in the nuclei over euchromatin and in axon terminals and lower levels of labeling in the neuropil, dendrites, and spines (Burette et al., 2017). The highest concentration in surgically resected human temporal cortical tissue was in euchromatin-rich domains in the nucleus, the head and neck of dendritic spines, although not the postsynaptic density, and in axon terminals of neuropil (Burette et al., 2018). Glial cells (GFAP+ astrocytes) showed intense nuclear and diffuse cytosolic staining of UBE3A, which was reduced but not completely diminished in AS-derived astrocytes (Grier et al., 2015); however, the labeling in neurons was much higher than in glial cells (Burette et al., 2017).

The presence of UBE3A protein in both the nucleus and cytosol reflects isoform-dependent subcellular localization (Fig. 1B). In both mouse and human tissue and cells, the short isoform (mUBE3A-iso3 and hUBE3A-iso1) is predominantly found in the nucleus

and expressed at approximately 4-fold greater levels than the long isoform(s), comprising around 75-80% of total UBE3A protein levels (Miao et al., 2013; Avagliano Trezza et al., 2019; Sirois et al., 2020; Zampeta et al., 2020; Judson et al., 2021). The longer isoform(s) (mUBE3A-iso2, hUBE3A-iso2, and hUBE3A-iso3) contribute ~20% to total UBE3A protein levels and mostly localize to the cytoplasm (Miao et al., 2013; Avagliano Trezza et al., 2019; Sirois et al., 2020; Zampeta et al., 2020; Judson et al., 2021; van Esbroeck et al., 2025). Of the two long human UBE3A isoforms, hUBE3A-iso3, which has a conserved sequence similar to mUBE3A-iso2, is much more highly expressed (~15-19%) than the long hUBE3A-iso2 (~1-2%) (Sirois et al., 2020; Judson et al., 2021). The relative abundance of the different isoforms at the protein level is consistent across development (Avagliano Trezza et al., 2019). Subcellular fractionation analysis of hESC-derived neurons indicates that, while the nucleus is highly enriched for hUBE3A-iso1, this isoform is present in all cellular compartments that were assayed and may be evenly distributed. Overall, the higher relative expression of isoform 1 derives from a combination of dense expression in the much smaller volume of the nucleus and sparse expression throughout the higher volume of the cytoplasm (Sirois et al., 2020).

The level of *Ube3a* expression and subcellular localization shift during neuronal maturation. Expression is present from the paternal allele during very early development in AS mouse neurons (Grier et al., 2015) and is detectable in human-derived cell culture (Leung et al., 2009); this likely explains why early development during the first few months of life is closer to neurotypical development. The amount of UBE3A protein expression present in cortical tissue of an AS mouse is much lower than WT levels, but distinctly present at birth and the first few days of postnatal development. This is due to expression from the not-yet-silent paternal allele during maturation, which then drops sharply during the first week and into adulthood (Sato and Stryker, 2010; Judson et al., 2014). Subcellular localization also changes during this early stage of development, as UBE3A protein expression shifts from primarily cytosolic and synaptic with more limited nuclear expression at P6 in both AS and WT mice to primarily nuclear-localized expression with less expression in the cytosol (Sato and Stryker, 2010; Judson et al., 2014).

Analysis of mRNA transcripts from the three different mouse isoforms (*mUbe3a*-iso1, -iso2, and -iso3) during development (embryonic day 15 to adulthood) showed that non-coding *mUbe3a*-iso1 and long *mUbe3a*-iso2 are expressed at much lower levels than the short *mUbe3a*-iso3, which was nearly 4-fold higher at E15 and ~2- to 10-fold higher than the murine isoforms 2 and 3 at P14, a ratio that persisted to adulthood (Fig. 1C) (Miao et al., 2013). Transcript levels from all three isoforms decreased during late embryonic and early postnatal development, although transcript levels were stable from P14 to adulthood (Miao et al., 2013). RNA-seq data from publicly available datasets confirmed this developmental trajectory of relative isoform expression in tissues collected throughout the brain (forebrain, hindbrain, and midbrain) with ~3- to 4-fold higher RNA transcripts for the short *mUbe3a*-iso3 than long *mUbe3a*-iso2 during embryonic development to birth, which shifted to ~1.6 :1 short *mUbe3a*-iso3 to long *mUbe3a*-iso2 across all tissues collected from adult mice (Judson et al., 2021).

Analysis of publicly available human RNA-seq data showed a consistent ratio of around 4:1 *hUBE3A*-iso1 (short) to *hUBE3A*-iso3 (long) with iso2 (long) expression at near zero during pre- and post-natal development and into adulthood in different regions of the brain (Fig. 1C) (Zampeta et al., 2020; Judson et al., 2021). In addition to maintenance of this isoform expression ratio across development, the *hUBE3A* RNA isoform expression ratios are maintained across different brain structures (pre-frontal and sensory cortices; deep brain structures, hippocampus and thalamus; and cerebellum) (Judson et al., 2021), which suggests that an expression ratio with a relative abundance of *hUBE3A*-iso1 transcripts may be important for normal neuronal function. Overall, there is a remarkable conservation of sequence, ratio of endogenous expression of isoforms, and subcellular localization across species for UBE3A.

UBE3A Function

E3 proteins, including UBE3A, are critical for substrate recognition as a component of the ubiquitination process for protein degradation (Yamamoto et al., 1997). UBE3A was first identified

for its role in degradation of the tumor suppressor protein p53 via the ubiquitination proteosome system through binding the viral E6 protein (Huibregtse et al., 1991, 1993). Identified targets of E6-AP include p53, p27, Arc, and ephexin5, proteins that are crucial for regulation of the nervous system at the cellular and synaptic level - disruption of these interactions can lead to neurologic deficits (Huibregtse et al., 1991; Mishra et al., 2009; Greer et al., 2010; Margolis et al., 2010; Sato and Stryker, 2010). A more extensive understanding of UBE3A's putative molecular functions in health and disease, interaction partners, and target substrates can be gained from recent reviews (Lopez et al., 2018; Khatri and Man, 2019; Biagioni et al., 2024; Krzeski et al., 2024; Yang and Huang, 2025).

It is well established that dysregulated UBE3A activity results in disease states such as Angelman syndrome (lack of maternal *UBE3A* expression) or Dup15q syndrome (extra maternal copy of *UBE3A*); the clinical hallmarks and genetic causes of AS are described in more detail in these reviews (Williams et al., 2010; Mabb et al., 2011; Tan et al., 2011; Dagli et al., 2012; Buiting et al., 2016). However, increasing evidence suggests that UBE3A exhibits isoform-specific biology with respect to molecular structure, subcellular localization, and interaction partners that may play distinct roles in health and disease states. Results from isogenic hESC-derived neuronal cultures support the finding that loss of the short, nuclear isoform (hUBE3A-iso1) alone is sufficient to cause AS-related phenotypes as the hUBE3A-iso1 knockout (KO) cell line showed a partial AS electrophysiological phenotype, with no changes in the hUBE3A-iso2/3 KO neurons (Sirois et al., 2020). The observed phenotype was less abnormal than in AS patient iPSC-derived neurons, suggesting that the presence of hUBE3A-iso2 and/or hUBE3A-iso3 can partially compensate in the absence of hUBE3A-iso1 (Sirois et al., 2020). Clinical data supports the criticality of the short, nuclear UBE3A isoform as a missense mutation has been identified in patients that interrupts the start codon of *hUBE3A*-iso1 (short nuclear) but not the *hUBE3A* isoforms 2 and 3 (long cytosolic), and results in AS, albeit with less severe symptoms (Sadhwani et al., 2018).

The p.Met1Thr start codon pathogenic variant in *hUBE3A*-iso1 was identified to result in improved communication, gait, and more advanced overall developmental skills than other AS individuals despite putative disruption of the more critical short nuclear isoform (Sadhwani et al., 2018). This mutation shifts localization of the next most abundant hUBE3A-iso3 from the cytosol to the nucleus. This site is sensitive to substitution, and p.Met21Ala or p.Met21Thr shifts hUBE3A isoform 3 localization from the cytosol to the nucleus in murine neuronal and U2-OS cell cultures, although the equivalent site in mUBE3A-Iso2 is much less sensitive to substitution (Zampeta et al., 2020; van Esbroeck et al., 2025). One potential explanation for the milder phenotype is that nuclear expression of hUBE3A-iso3 can functionally compensate for the loss of hUBE3A-iso1. However, it is unknown whether this shift in subcellular localization impacts catalytic activity, and differences in N-terminal extension and isoform structure may limit binding with substrates that typically interact with isoform 1.

Bossuyt et al. screened 31 UBE3A missense mutations in neuronal cultures for disruptions in subcellular localization, catalytic activity, and stability and found the majority of the variants tested (55%) caused mislocalization with partial or complete loss of nuclear UBE3A and appearance of UBE3A signal in the cytosol (Bossuyt et al., 2021). All mislocalized variants also showed reduced UBE3A protein levels, likely due to incorrect folding, instability, and quicker degradation, which contrasted with the general characteristics of variants that maintained nuclear localization and typically resulted in reduced catalytic activity and increased amounts of UBE3A (Bossuyt et al., 2021) (see Fig. 5 in Bossuyt et al., 2021 for schematic overview of the location and classification of UBE3A missense mutations assessed). A limited number of variants have been identified that showed correct nuclear localization, normal ubiquitination, and normal or increased UBE3A levels in neuronal culture that have also been identified in individuals with milder neurodevelopmental delays that did not meet the criteria for AS (pAsn340del; p.Asp563Gly) or may be benign variants (p.Leu273Arg; p. Arg626Pro) (Bai et al., 2014; Geerts-Haages et al., 2020).

The functional contributions of different UBE3A isoforms to AS-related phenotypes have been dissected using *Ube3a* isoform-specific KO mice (Avagliano Trezza et al., 2019), isogenic hESCs

(Sirois et al., 2020), and isoform-specific hiPSC-derived neurons (Zampeta et al., 2020). Loss of the short, nuclear, and more abundant *mUbe3a*-iso3 resulted in a greater reduction of UBE3A protein expression and behavioral deficits similar to AS mice, including decreased rotarod performance, decreased nest-building material used, decreased marble burying, and increased time floating during forced-swim test, while the *mUbe3a*-iso2 KO performed similar to WT mice (Avagliano Trezza et al., 2019). Loss of *mUbe3A*-iso3 in the KO also resulted in synaptic changes indicative of disruption to the excitation-to-inhibition balance, suggesting that loss of the short, nuclear *Ube3a* isoform results in increased seizure susceptibility and that its expression is critical for maintaining stable electrical activity (Avagliano Trezza et al., 2019).

Expression of the non-coding mouse *Ube3a*-iso1 transcript is regulated by neuronal activity and enriched in the dendritic compartment. The *mUbe3a*-iso1 mRNA transcripts play a role in regulating the complexity of dendrites and spine morphology, even in the absence of protein expression, by pruning dendritic complexity and promoting spine maturation in opposition to *mUbe3a*-iso2/-iso3, which increased dendritic complexity (Valluy et al., 2015).

Downregulation of *Ube3a* in pyramidal neurons revealed an important role for the long cytosolic isoform (*mUbe3a*-iso2) in neural development, as rescue of inhibited apical dendrite outgrowth and impaired dendrite polarity was only found with expression of *mUbe3a*-iso2 (homolog of *hUBE3A*-iso3), while coexpression with isoform 1 or 3 failed to achieve rescue (Miao et al., 2013). However, it is clear from other studies that the dosage of mUBE3A-iso2 protein levels must be within a limited physiological range as neuronal overexpression of the cytosolic isoform *mUbe3a*-iso2 in mice caused anxiety-like behaviors, learning impairments, and reduced seizure threshold in addition to neuroanatomical pathology including large reductions in forebrain, hippocampus, striatum, amygdala, and cortical volume in line with phenotypes associated with Dup15q syndrome (Copping et al., 2017). One caveat is that the Tetracycline-Off system used to overexpress *mUbe3a*-iso2 targeted excitatory neurons due to the CamKIIa promotor used, and it is possible that imbalanced UBE3A expression among excitatory and inhibitory forebrain neurons contributed to an exacerbation of seizure phenotypes, as demonstrated in conditional *Ube3a* deletion experiments that showed selective loss of *Ube3a* from GABAergic neurons increased seizure susceptibility and EEG activity characteristic of AS (Judson et al., 2016).

Numerous efforts have been led to characterize the interacting partners of UBE3A. Krzeski et al. outlined potential UBE3A substrates and their subcellular localization in neurons (nucleus, cytoplasm, plasma membrane, dendrites, synapses, or mitochondria) (Krzeski et al., 2024). Martínez-Noël et al. used a proteomic approach using wildtype, dominant negative, and catalytically inactive versions of all the UBE3A isoforms to identify substrate interactions and characterize isoform-specific differences using T-Rex 293 or SH-SY5Y cell lines or a yeast two-hybrid screen (Martínez-Noël et al., 2012; Martínez-Noël et al., 2018). Although isoform 1 more efficiently pulled down proteasome subunits, there was a great extent of overlap across all three isoforms with the most unique potential interactions identified for isoform 2, suggesting there is redundancy across the isoforms to bind as part of protein complexes (Martínez-Noël et al., 2012; Martínez-Noël et al., 2018). It is also feasible that the relative abundance in a physiological setting would impact the availability of different isoforms and likelihood for direct or indirect substrate recognition/binding affinity. These findings of high overlap for potential substrate interactions across all isoforms with a limited number of unique interaction partners identified for individual isoforms may be due to differences in structural and/or biophysical properties.

Analytical testing to understand the structure, conformational dynamics, and interactions of the three hUBE3A isoforms demonstrated that some structural features, such as the AZUL domain structure and association with Rpn10, were consistent across all isoforms (Bregnard et al., 2025). However, sequence-dependent differences have also been identified. The two long isoforms (hUBE3A-iso2 and -iso3) have an extended N-terminal helix and are able to dimerize, a feature which may be responsible for oligomerization-dependent activation of the UBE3A, whereas only hUBE3A-iso1 and -iso3 contain a dynamic Zn-coordination site, which may contribute to an isoform-specific sensitivity to oxidative stress (Bregnard et al.,

2025), and may facilitate hUBE3A-iso3 compensation in the absence of hUBE3A-iso1. The unique combination of biophysical characteristics for each isoform and differences in N-terminal flexibility, conformational dynamics, and multimerization may result in differences in stability/turnover, subcellular localization, and interactomes (Bregnard et al., 2025).

Dysregulation of substrate binding significantly impacts neuronal processes and overall brain function as loss-of-function point mutations in the HECT domain can result in AS (Cooper et al., 2004; Yi et al., 2015). Work in neuronal cultures identified the direct interaction between PSMD4, a subunit of the 19S regulatory particle of the 26S proteasome, and the AZUL domain of UBE3A is required for nuclear targeting and facilitates binding the proteasome (Avagliano Trezza et al., 2019). This interaction is responsible for nuclear targeting, nuclear import, and retention in the nucleus; disruptions of the AZUL-PSMD4 binding through a missense mutation results in cytosolic expression and can result in AS presentation (Avagliano Trezza et al., 2019). While all isoforms contain this domain, the interaction between PSMD4 and the AZUL domain in the short nuclear isoform (mUBE3A-iso3) directly at the N-terminus leads to nuclear localization, and missense mutations in the AZUL domain (i.e., p.Cys21Tyr, p.Gly20Val) result in expression solely in the cytosol due to a lack of nuclear retention controlled by the zinc finger within the AZUL domain (Avagliano Trezza et al., 2019).

The prevailing data indicate that nuclear UBE3A plays a critical role in normal physiological function and that loss of the short nuclear isoform (hUBE3A-iso1 or mUBE3A-iso3) negatively impacts behavior and electrical activity in mouse models and cellular function in human-derived neurons. While cytosolic long UBE3A likely contributes to normal function, the presence of, or an increase in, long cytosolic UBE3A isoforms does not appear to be sufficient to compensate for the loss of nuclear UBE3A. It is currently unclear what the impact of selective loss of hUBE3A-iso2 or hUBE3A-iso3 would be in a developing human. Evidently identifying and characterizing the molecular and clinical features of isoform-specific UBE3A missense mutations - the second most common cause of AS cases (10-15%) - would inform our understanding of UBE3A biology (Malzac et al., 1998). Critically, it appears that replacement of nuclear UBE3A could improve clinical outcomes.

UBE3A Isoforms and Therapeutic Strategies

There are currently no approved disease-modifying treatments for AS; however, recent years have seen encouraging developments. A handful of investigational products have reached the clinical stage, including three antisense oligonucleotides (ASOs) that disrupt the paternal imprinting process to reinstate UBE3A expression from the normally silenced paternal allele and are at the Phase III clinical trial phase, and an AAV-*hUBE3A*-iso1-mediated gene replacement therapy is positioned to start enrollment for a Phase I/II trial. Phase 1 clinical trial data from the ASO Rugonerson (RO7248824) has provided proof-of-concept for safety, tolerability, and clinical improvements by increasing UBE3A expression in AS individuals (Hipp et al., 2025). For more in-depth reviews on current and future therapeutic development in AS, see (Markati et al., 2021) and (Copping et al., 2021).

The importance of different UBE3A isoforms in the rescue of AS clinical features can be informed by preclinical animal model studies that have used isoform-specific approaches to restore UBE3A expression to the brain. Achieving even limited amounts of UBE3A expression may enable clinically meaningful improvements as suggested by the milder clinical features seen in AS individuals with as few as 1% of cells expressing UBE3A due to mosaicism (Brockmann et al., 2002; Nazlican et al., 2004; Le Fevre et al., 2017). It will be important to understand whether manipulating the expression of any individual isoform affects the expression of the other isoforms for a given therapeutic strategy. The generation of conditional *Ube3a* overexpressing mice with an additional 1, 2, or 4 copies of *Ube3a* demonstrated similar ratios of short: long *mUbe3a* isoform expression, indicating that overexpression does not result in changes to the relative expression of either isoform (Punt et al., 2022). Additionally, removal of specific *hUBE3A* isoforms in hESC-derived neurons also does not appear to disrupt the production or localization of the remaining isoforms, suggesting

they are processed independently of each other (Sirois et al., 2020).

The first proof-of-concept study for treatment of AS with gene or protein replacement delivered AAV9-*mUbe3a*-iso3 with a ubiquitous promoter to adult AS mice via direct bilateral hippocampal injections (Jiang et al., 1998; Daily et al., 2011). This intervention successfully increased UBE3A expression to WT levels in the hippocampus and improved some AS-relevant phenotypes compared with AAV-GFP injected control mice, including associative learning and memory and supported partial recovery of hippocampal synaptic plasticity as assessed by long-term potentiation (LTP) (Daily et al., 2011). However, expression of the transgene was limited in distribution and was not present in other regions of the brain important for neurological function, such as the cerebellum, which likely explains the lack of rescue in motor deficits and overall partial rescue (Daily et al., 2011).

Administration of an engineered construct including *hUBE3A*-iso1 in combination with a secretion signal and cell-penetrating peptide sequence to adult AS mice or AS rats either directly to the hippocampus or by ICV injection to target a broader distribution of isoform 1 protein expression outside of the AAV-mediated transduction resulted in improvements in associative memory, motor learning, and LTP (Nenninger et al., 2022). Delivery of the short nuclear isoform (hUBE3A-iso1 or mUBE3A-iso3) to neonatal and young adult immunodeficient AS mice using a lentivector-transduced hematopoietic stem cell system also showed promising improvements in AS-relevant behavioral phenotypes (Adhikari et al., 2021). A direct protein replacement strategy using recombinant human UBE3A-iso1 protein delivered bilaterally directly to the hippocampus in adult rats was also able to improve associative memory and LTP (Dodge et al., 2022). Together these findings support that expression of *hUBE3A*-iso1 is sufficient to improve functional and neurophysiological outcomes.

More recent work from Judson et al. used a dual-isoform neuronal-specific PHP.B-*hUBE3A* vector administered ICV to neonates with different strength Kozak sequences to bias expression towards short (*hUBE3A*-iso1) over long (*hUBE3A*-iso3) isoforms close to the short:long isoform ratio seen in wildtype mice (~3.5:1 short to long in WT mice, ~2.7:1 in AAV-dual isoform) and across human development (Judson et al., 2021). This strategy resulted in broad protein expression throughout the brain that significantly improved motor learning and mouse-specific behaviors in AS mice as well as decreased seizure susceptibility and kindling-associated hippocampal pathology (Judson et al., 2021). In the absence of a side-by-side comparison using the same capsid and promoter, it is currently unclear whether the combined dual-isoform strategy is more effective than *hUBE3A*-iso1 or *hUBE3A*-iso3 alone.

Long cytosolic isoforms (hUBE3A-iso2, -iso3) play a role in neural development and may be able to compensate for loss of isoform 1 to some degree, but a strategy relying solely on *hUBE3A*-iso3/*mUbe3a*-iso2 expression may be less effective and risk exacerbating phenotypes or precipitating deleterious outcomes when overexpressed too highly (Copping et al., 2017). It is unclear why overexpression of the long isoform is associated with a greater risk of adverse outcomes, but this could reflect isoform-specific molecular dynamics pertaining to turnover/stability, catalytic activity, and/or subcellular localization. Further studies manipulating the relative expression of each isoform could provide useful insights relating to disease pathology or highlight therapeutic strategies to avoid.

It is assumed that ASO treatment, by virtue of targeting the native *UBE3A-ATS*, is isoform-agnostic and results in a balanced expression ratio of all three isoforms similar to the endogenous ratio, although this is not yet known. It is also unknown what ratio of isoform expression is most beneficial to individuals with AS and whether ASOs could be engineered to achieve the optimal therapeutic isoform ratio. Furthermore, it is unclear whether an isoform-specific strategy might lead to better outcomes for a subset within the heterologous AS population, including missense mutations that may have variable isoform-specific effects. It will also be important to consider how the stage of neuronal development at the time of treatment may be impacted by isoform-specific changes that occur during development.

Earlier treatment is generally associated with better outcomes, such that very early *in utero* or post-natal timepoints have been proposed to achieve more

effective rescue of AS by restoring *UBE3A* expression during critical developmental windows and allowing for lower payloads of therapeutic agent (Schwab and MacKenzie, 2021; Clarke et al., 2024). Future studies should seek to better understand isoform-dependent functions and protein-protein interactions that could inform therapeutic strategies through identification or optimization of new small molecule drugs or putative biomarkers.

Conclusion

UBE3A exhibits isoform-dependent differences in expression levels, subcellular localization, structure, and substrate interactions that can change during development. Current data indicate that hUBE3A-iso1 is essential for neuronal physiology and behavioral function and support prioritizing therapeutic strategies relying on expression of this isoform, or that express hUBE3A-iso1 with hUBE3A-iso3 at close to the 4:1 endogenous ratio. As the field enters the next stage of therapeutic development, it will be necessary to obtain a deeper understanding of how the different UBE3A isoforms are expressed and function in normal neurons to guide future therapeutic strategies.

Conflict of Interest

H.B. is currently an employee of GEMMA Biotherapeutics.

References

Adhikari A, Copping NA, Beegle J, Cameron DL, Deng P, O'Geen H, Segal DJ, Fink KD, Silverman JL, Anderson JS (2021) Functional rescue in an Angelman syndrome model following treatment with lentivector transduced hematopoietic stem cells. Hum Mol Genet 30:1067-1083.

Avagliano Trezza R, Sonzogni M, Bossuyt SNV, Zampeta FI, Punt AM, van den Berg M, Rotaru DC, Koene LMC, Munshi ST, Stedehouder J, Kros JM, Williams M, Heussler H, de Vrij FMS, Mientjes EJ, van Woerden GM, Kushner SA, Distel B, Elgersma Y (2019) Loss of nuclear UBE3A causes electrophysiological and behavioral deficits in mice and is associated with Angelman syndrome. Nat Neurosci 22:1235-1247.

Bai JL, Qu YJ, Jin YW, Wang H, Yang YL, Jiang YW, Yang XY, Zou LP, Song F (2014) Molecular and clinical characterization of Angelman syndrome in Chinese patients. Clin Genet 85:273-277.

Biagioni M, Baronchelli F, Fossati M (2024) Multiscale spatio-temporal dynamics of UBE3A gene in brain physiology and neurodevelopmental disorders. Neurobiol Dis 201:106669.

Bossuyt SNV, Punt AM, de Graaf IJ, van den Burg J, Williams MG, Heussler H, Elgersma Y, Distel B (2021) Loss of nuclear UBE3A activity is the predominant cause of Angelman syndrome in individuals carrying UBE3A missense mutations. Hum Mol Genet 30:430-442.

Bregnard TA, Fairchild D, Chen X, Erlandsen H, Tarasov SG, Walters KJ, Korzhnev DM, Bezsonova I (2025) Differences in structure, dynamics, and zinc coordination between isoforms of human ubiquitin ligase UBE3A. J Biol Chem 301:108149.

Brockmann K, Böhm R, Bürger J (2002) Exceptionally mild Angelman syndrome phenotype associated with an incomplete imprinting defect. J Med Genet 39:e51.

Buiting K, Williams C, Horsthemke B (2016) Angelman syndrome - insights into a rare neurogenetic disorder. Nat Rev Neurol 12:584-593.

Buiting K, Saitoh S, Gross S, Dittrich B, Schwartz S, Nicholls RD, Horsthemke B (1995) Inherited microdeletions in the Angelman and Prader-Willi syndromes define an imprinting centre on human chromosome 15. Nat Genet 9:395-400.

Burette AC, Judson MC, Burette S, Phend KD, Philpot BD, Weinberg RJ (2017) Subcellular organization of UBE3A in neurons. J Comp Neurol 525:233-251.

Burette AC, Judson MC, Li AN, Chang EF, Seeley WW, Philpot BD, Weinberg RJ (2018) Subcellular organization of UBE3A in human cerebral cortex. Mol Autism 9:54.

Clarke MT, Remesal L, Lentz L, Tan DJ, Young D, Thapa S, Namuduri SR, Borges B, Kirn G, Valencia J, Lopez ME, Lui JH, Shiow LR, Dindot S, Villeda S, Sanders SJ, MacKenzie TC (2024) Prenatal delivery of a therapeutic antisense oligonucleotide achieves broad biodistribution in the brain and ameliorates Angelman syndrome phenotype in mice. Mol Ther 32:935-951.

Cooper EM, Hudson AW, Amos J, Wagstaff J, Howley PM (2004) Biochemical analysis of Angelman syndrome-associated mutations in the

E3 ubiquitin ligase E6-associated protein. J Biol Chem 279:41208-41217.

Copping NA, McTighe SM, Fink KD, Silverman JL (2021) Emerging Gene and Small Molecule Therapies for the Neurodevelopmental Disorder Angelman Syndrome. Neurotherapeutics 18:1535-1547.

Copping NA, Christian SGB, Ritter DJ, Islam MS, Buscher N, Zolkowska D, Pride MC, Berg EL, LaSalle JM, Ellegood J, Lerch JP, Reiter LT, Silverman JL, Dindot SV (2017) Neuronal overexpression of Ube3a isoform 2 causes behavioral impairments and neuroanatomical pathology relevant to 15q11.2-q13.3 duplication syndrome. Hum Mol Genet 26:3995-4010.

Dagli A, Buiting K, Williams CA (2012) Molecular and Clinical Aspects of Angelman Syndrome. Mol Syndromol 2:100-112.

Daily JL, Nash K, Jinwal U, Golde T, Rogers J, Peters MM, Burdine RD, Dickey C, Banko JL, Weeber EJ (2011) Adeno-associated virus-mediated rescue of the cognitive defects in a mouse model for Angelman syndrome. PLoS One 6:e27221.

Dindot SV, Antalffy BA, Bhattacharjee MB, Beaudet AL (2008) The Angelman syndrome ubiquitin ligase localizes to the synapse and nucleus, and maternal deficiency results in abnormal dendritic spine morphology. Hum Mol Genet 17:111-118.

Dodge A, Morrill NK, Weeber EJ, Nash KR (2022) Recovery of Angelman syndrome rat deficits with UBE3A protein supplementation. Mol Cell Neurosci 120:103724.

Fiumara A, Pittalà A, Cocuzza M, Sorge G (2010) Epilepsy in patients with Angelman syndrome. Ital J Pediatr 36:31.

Geerts-Haages A, Bossuyt SNV, den Besten I, Bruggenwirth H, van der Burgt I, Yntema HG, Punt AM, Brooks A, Elgersma Y, Distel B, Valstar M (2020) A novel UBE3A sequence variant identified in eight related individuals with neurodevelopmental delay, results in a phenotype which does not match the clinical criteria of Angelman syndrome. Mol Genet Genomic Med 8:e1481.

Greer PL, Hanayama R, Bloodgood BL, Mardinly AR, Lipton DM, Flavell SW, Kim TK, Griffith EC, Waldon Z, Maehr R, Ploegh HL, Chowdhury S, Worley PF, Steen J, Greenberg ME (2010) The Angelman Syndrome protein Ube3A regulates synapse development by ubiquitinating arc. Cell 140:704-716.

Grier MD, Carson RP, Lagrange AH (2015) Toward a Broader View of Ube3a in a Mouse Model of Angelman Syndrome: Expression in Brain, Spinal Cord, Sciatic Nerve and Glial Cells. PLoS One 10:e0124649.

Gustin RM, Bichell TJ, Bubser M, Daily J, Filonova I, Mrelashvili D, Deutch AY, Colbran RJ, Weeber EJ, Haas KF (2010) Tissue-specific variation of Ube3a protein expression in rodents and in a mouse model of Angelman syndrome. Neurobiol Dis 39:283-291.

Hipp JF et al. (2025) The UBE3A-ATS antisense oligonucleotide rugonersen in children with Angelman syndrome: a phase 1 trial. Nat Med 31:2936-2945.

Huibregtse JM, Scheffner M, Howley PM (1991) A cellular protein mediates association of p53 with the E6 oncoprotein of human papillomavirus types 16 or 18. Embo j 10:4129-4135.

Huibregtse JM, Scheffner M, Howley PM (1993) Localization of the E6-AP regions that direct human papillomavirus E6 binding, association with p53, and ubiquitination of associated proteins. Mol Cell Biol 13:4918-4927.

Jana NR (2012) Understanding the pathogenesis of Angelman syndrome through animal models. Neural Plast 2012:710943.

Jiang YH, Armstrong D, Albrecht U, Atkins CM, Noebels JL, Eichele G, Sweatt JD, Beaudet AL (1998) Mutation of the Angelman ubiquitin ligase in mice causes increased cytoplasmic p53 and deficits of contextual learning and long-term potentiation. Neuron 21:799-811.

Judson MC, Sosa-Pagan JO, Del Cid WA, Han JE, Philpot BD (2014) Allelic specificity of Ube3a expression in the mouse brain during postnatal development. J Comp Neurol 522:1874-1896.

Judson MC, Wallace ML, Sidorov MS, Burette AC, Gu B, van Woerden GM, King IF, Han JE, Zylka MJ, Elgersma Y, Weinberg RJ, Philpot BD (2016) GABAergic Neuron-Specific Loss of Ube3a Causes Angelman Syndrome-Like EEG Abnormalities and Enhances Seizure Susceptibility. Neuron 90:56-69.

Judson MC, Shyng C, Simon JM, Davis CR, Punt AM, Salmon MT, Miller NW, Ritola KD, Elgersma Y, Amaral DG, Gray SJ, Philpot BD (2021) Dual-

isoform hUBE3A gene transfer improves behavioral and seizure outcomes in Angelman syndrome model mice. JCI Insight 6.

Kaphzan H, Hernandez P, Jung JI, Cowansage KK, Deinhardt K, Chao MV, Abel T, Klann E (2012) Reversal of impaired hippocampal long-term potentiation and contextual fear memory deficits in Angelman syndrome model mice by ErbB inhibitors. Biol Psychiatry 72:182-190.

Khatri N, Man HY (2019) The Autism and Angelman Syndrome Protein Ube3A/E6AP: The Gene, E3 Ligase Ubiquitination Targets and Neurobiological Functions. Front Mol Neurosci 12:109.

Kishino T, Lalande M, Wagstaff J (1997) UBE3A/E6-AP mutations cause Angelman syndrome. Nat Genet 15:70-73.

Krzeski JC, Judson MC, Philpot BD (2024) Neuronal UBE3A substrates hold therapeutic potential for Angelman syndrome. Curr Opin Neurobiol 88:102899.

Kühnle S, Kogel U, Glockzin S, Marquardt A, Ciechanover A, Matentzoglu K, Scheffner M (2011) Physical and functional interaction of the HECT ubiquitin-protein ligases E6AP and HERC2. J Biol Chem 286:19410-19416.

Le Fevre A, Beygo J, Silveira C, Kamien B, Clayton-Smith J, Colley A, Buiting K, Dudding-Byth T (2017) Atypical Angelman syndrome due to a mosaic imprinting defect: Case reports and review of the literature. Am J Med Genet A 173:753-757.

Leung KN, Vallero RO, DuBose AJ, Resnick JL, LaSalle JM (2009) Imprinting regulates mammalian snoRNA-encoding chromatin decondensation and neuronal nucleolar size. Hum Mol Genet 18:4227-4238.

Lopez SJ, Segal DJ, LaSalle JM (2018) UBE3A: An E3 Ubiquitin Ligase With Genome-Wide Impact in Neurodevelopmental Disease. Front Mol Neurosci 11:476.

Mabb AM, Judson MC, Zylka MJ, Philpot BD (2011) Angelman syndrome: insights into genomic imprinting and neurodevelopmental phenotypes. Trends Neurosci 34:293-303.

Malzac P, Webber H, Moncla A, Graham JM, Kukolich M, Williams C, Pagon RA, Ramsdell LA, Kishino T, Wagstaff J (1998) Mutation analysis of UBE3A in Angelman syndrome patients. Am J Hum Genet 62:1353-1360.

Margolis SS, Sell GL, Zbinden MA, Bird LM (2015) Angelman Syndrome. Neurotherapeutics 12:641-650.

Margolis SS, Salogiannis J, Lipton DM, Mandel-Brehm C, Wills ZP, Mardinly AR, Hu L, Greer PL, Bikoff JB, Ho HY, Soskis MJ, Sahin M, Greenberg ME (2010) EphB-mediated degradation of the RhoA GEF Ephexin5 relieves a developmental brake on excitatory synapse formation. Cell 143:442-455.

Markati T, Duis J, Servais L (2021) Therapies in preclinical and clinical development for Angelman syndrome. Expert Opin Investig Drugs 30:709-720.

Martínez-Noël G, Galligan JT, Sowa ME, Arndt V, Overton TM, Harper JW, Howley PM (2012) Identification and proteomic analysis of distinct UBE3A/E6AP protein complexes. Mol Cell Biol 32:3095-3106.

Martínez-Noël G, Luck K, Kühnle S, Desbuleux A, Szajner P, Galligan JT, Rodriguez D, Zheng L, Boyland K, Leclere F, Zhong Q, Hill DE, Vidal M, Howley PM (2018) Network Analysis of UBE3A/E6AP-Associated Proteins Provides Connections to Several Distinct Cellular Processes. J Mol Biol 430:1024-1050.

Matsuura T, Sutcliffe JS, Fang P, Galjaard RJ, Jiang YH, Benton CS, Rommens JM, Beaudet AL (1997) De novo truncating mutations in E6-AP ubiquitin-protein ligase gene (UBE3A) in Angelman syndrome. Nat Genet 15:74-77.

Miao S, Chen R, Ye J, Tan GH, Li S, Zhang J, Jiang YH, Xiong ZQ (2013) The Angelman syndrome protein Ube3a is required for polarized dendrite morphogenesis in pyramidal neurons. J Neurosci 33:327-333.

Mishra A, Godavarthi SK, Jana NR (2009) UBE3A/E6-AP regulates cell proliferation by promoting proteasomal degradation of p27. Neurobiol Dis 36:26-34.

Nazlican H, Zeschnigk M, Claussen U, Michel S, Boehringer S, Gillessen-Kaesbach G, Buiting K, Horsthemke B (2004) Somatic mosaicism in patients with Angelman syndrome and an imprinting defect. Hum Mol Genet 13:2547-2555.

Nenninger AW, Willman M, Willman J, Stewart E, Mesidor P, Novoa M, Morrill NK, Alvarez L, Joly-Amado A, Peters MM, Gulick D, Nash KR (2022) Improving Gene Therapy for Angelman Syndrome

with Secreted Human UBE3A. Neurotherapeutics 19:1329-1339.

Punt AM, Judson MC, Sidorov MS, Williams BN, Johnson NS, Belder S, den Hertog D, Davis CR, Feygin MS, Lang PF, Jolfaei MA, Curran PJ, van IWF, Elgersma Y, Philpot BD (2022) Molecular and behavioral consequences of Ube3a gene overdosage in mice. JCI Insight 7.

Sadhwani A, Sanjana NE, Willen JM, Calculator SN, Black ED, Bean LJH, Li H, Tan WH (2018) Two Angelman families with unusually advanced neurodevelopment carry a start codon variant in the most highly expressed UBE3A isoform. Am J Med Genet A 176:1641-1647.

Sato M, Stryker MP (2010) Genomic imprinting of experience-dependent cortical plasticity by the ubiquitin ligase gene Ube3a. Proc Natl Acad Sci U S A 107:5611-5616.

Scheffner M, Huibregtse JM, Howley PM (1994) Identification of a human ubiquitin-conjugating enzyme that mediates the E6-AP-dependent ubiquitination of p53. Proc Natl Acad Sci U S A 91:8797-8801.

Schwab ME, MacKenzie TC (2021) Prenatal Gene Therapy. Clin Obstet Gynecol 64:876-885.

Sirois CL, Bloom JE, Fink JJ, Gorka D, Keller S, Germain ND, Levine ES, Chamberlain SJ (2020) Abundance and localization of human UBE3A protein isoforms. Hum Mol Genet 29:3021-3031.

Tan WH, Bacino CA, Skinner SA, Anselm I, Barbieri-Welge R, Bauer-Carlin A, Beaudet AL, Bichell TJ, Gentile JK, Glaze DG, Horowitz LT, Kothare SV, Lee HS, Nespeca MP, Peters SU, Sahoo T, Sarco D, Waisbren SE, Bird LM (2011) Angelman syndrome: Mutations influence features in early childhood. Am J Med Genet A 155a:81-90.

Valluy J, Bicker S, Aksoy-Aksel A, Lackinger M, Sumer S, Fiore R, Wüst T, Seffer D, Metge F, Dieterich C, Wöhr M, Schwarting R, Schratt G (2015) A coding-independent function of an alternative Ube3a transcript during neuronal development. Nat Neurosci 18:666-673.

Van Buggenhout G, Fryns JP (2009) Angelman syndrome (AS, MIM 105830). Eur J Hum Genet 17:1367-1373.

van Esbroeck ACM, Verhagen RFM, Biagioni M, Fossati M, Distel B, Elgersma Y (2025) Localization of human UBE3A isoform 3 is highly sensitive to amino acid substitutions at p.Met21 position. Hum Mol Genet 34:1009-1016.

Wang T, van Woerden GM, Elgersma Y, Borst JGG (2017) Enhanced Transmission at the Calyx of Held Synapse in a Mouse Model for Angelman Syndrome. Front Cell Neurosci 11:418.

Williams CA, Driscoll DJ, Dagli AI (2010) Clinical and genetic aspects of Angelman syndrome. Genet Med 12:385-395.

Yamamoto Y, Huibregtse JM, Howley PM (1997) The human E6-AP gene (UBE3A) encodes three potential protein isoforms generated by differential splicing. Genomics 41:263-266.

Yang X, Huang YA (2025) Unraveling the Roles of UBE3A in Neurodevelopment and Neurodegeneration. Int J Mol Sci 26.

Yi JJ, Berrios J, Newbern JM, Snider WD, Philpot BD, Hahn KM, Zylka MJ (2015) An Autism-Linked Mutation Disables Phosphorylation Control of UBE3A. Cell 162:795-807.

Zampeta FI, Sonzogni M, Niggl E, Lendemeijer B, Smeenk H, de Vrij FMS, Kushner SA, Distel B, Elgersma Y (2020) Conserved UBE3A subcellular distribution between human and mice is facilitated by non-homologous isoforms. Hum Mol Genet 29:3032-3043.

fast DART
DATA, ANALYSIS, REVIEWS, TECHNIQUES E-JOURNAL

Biotechniques

Delivery of Recombinant Adeno-Associated Virus into the Rodent Brain

Marselina Levis Rabi [1#], Natalia Hurst-Calle [1#], Jonathan Willman [1^], Matthew Willman [1^], Casey Cook [2], Aurelie Joly-Amado [1] and Kevin R. Nash [1*]

[1]Department of Molecular Pharmacology and Physiology, Morsani College of Medicine, University of South Florida (USF)
[2]Molecular Medicine Department, Morsani College of Medicine, University of South Florida
[#]Co-first author (contributed equally)
[^]Contributed while at USF but currently at University of Florida, Department of Surgery
[*]Corresponding Author: Kevin Nash, nash@usf.edu

Article History
Submitted: September 18, 2025 Accepted: October 24, 2025 Published: November 1, 2025

Abstract
Recombinant adeno-associated virus (rAAV) has emerged as a powerful and versatile tool for manipulating gene expression in the central nervous system of experimental animals. Its utility stems from a favorable safety profile, capacity for long-term transgene expression, and ability to target specific cell types depending on serotype and promoter selection. Given the recent FDA approval of AAV for clinical use, its application in preclinical models is now even more relevant and translational, reinforcing its value in bridging experimental research and therapeutic development. In this article, we present a comprehensive overview of methodologies for rAAV-mediated gene delivery to the rodent brain. We detail protocols for intracranial, intra-cisterna magna and intravenous administration.

Keywords: Recombinant adeno-associated virus (rAAV), Central nervous system, Gene Therapy, Stereotaxy, Intracerebroventricular, Intravenous, Retroorbital, Rodent

Introduction

Recombinant adeno-associated virus (rAAV) vectors have become indispensable tools for gene delivery in therapeutic applications. Several key advantages include a strong safety profile, the potential for long-term transgene expression, and the ability to selectively target specific cell populations through strategic serotype and promoter selection (Matuszek et al., 2025; Wang and Xiao, 2025). Some vectors are injected directly into the brain parenchyma for optimal efficiency, while others can access deep brain regions via ventricular administration. In addition, some serotypes enable recombinant adeno-associated virus (rAAV) to reach the brain following systemic vascular injection (Goertsen et al., 2022; Matuszek et al., 2025; Wang and Xiao, 2025). rAAV is generally considered to be safe and non-pathogenic and exhibits a favorable immune response compared to other vectors while allowing sustained and stable protein expression (Ling et al., 2023). The durability of rAAV-mediated expression has been well documented, with transgene activity persisting over 1.5 years in rodents and up to 6 years in non-human primates (Ideno et al., 2003; Rivera et al., 2005). Notably, the therapeutic effect of Voretigene neparvovec (Luxterna), an AAV based gene therapy medication for the treatment of Leber congenital amaurosis, has lasted for at least a decade

in animal models and 7.5 years in human patients (Leroy et al., 2023). In our own studies, transgene expression is typically detectable within one week of injection and stabilizes within 3 to 4 weeks, and remains consistent until euthanasia; we have performed studies ranging from 3 months to 9 months post-injection (Carty et al., 2013; Nenninger et al., 2022; Gorzek et al., 2025).

In rodent models, rAAV vectors can be administered via multiple routes, each offering distinct advantages depending on the target region and desired expression profile. Direct intracranial injection allows for precise targeting of brain structures, intra-cisterna magna delivery enables widespread CNS distribution, and intravenous injection provides a minimally invasive alternative capable of reaching the brain under specific conditions (Wang and Xiao, 2025).

This article presents a comprehensive overview of stereotaxic and non-stereotaxic techniques for rAAV-mediated gene delivery to the rodent brain, including detailed protocols for intracranial, intra-cisterna magna, and intravenous administration.

NOTE: All procedures involving live animals must be reviewed and approved by the appropriate institutional ethics committee and must adhere to established guidelines for the care and use of laboratory animals.

NOTE: Stereotaxic survival surgeries should be conducted using sterile techniques to ensure aseptic conditions.

NOTE: Rooms and procedures must adhere to specific biosafety and facility standards to ensure safety for personnel, animals, and the environment and follow the institutional biosafety committees (IBC) requirements.

Materials & Supplies

General Supplies

- Recombinant AAV vector (properly titered and stored)
- Sterile PBS or vehicle solution
- Ice bucket or cold block (for keeping virus cold)
- Timer or stopwatch
- Electric clippers/trimmers
- Heating pad (to maintain body temperature)
- Sterile gloves
- Animal identification tags or markers
- Institutional Animal Care and Use Committee (IACUC) protocol approval
- Documentation of aseptic technique for survival surgeries
- Biohazard disposal

Stereotaxic Injection

- Stereotaxic frame with digital controllers [World Precision Instruments 505322]
- Mouse adaptor [Kopf Model 923-B]
- Rat adaptor [Kopf Model 920]
- Rat anesthesia mask (Kopf Model 906)
- Anesthesia induction chamber [Patterson Scientific 78933387]
- Hamilton syringe [Hamilton 81022]
- Microdrill [RWD Life Sciences 78001]
- Microinjector [World Precision Instruments UMP3]
- Anesthesia system (e.g., isoflurane vaporizer) [Matrx 94805059]
- Oxygen tank [Airgas Healthcare UN1072]
- Oxygen pressure regulator [Western Medica 96-M2-540-P]
- Isoflurane [Piramal 66794-017-25]
- Surgical tools (scissors, forceps, scalpel, mosquito hemostats)
- Sterilized cotton swabs [Fisher Scientific 23-400-124]
- Bead sterilizer (for sterilization of surgical tools) [Braintree Scientific GER5287120V]
- Surgical drapes [Dynarex 4410]
- Iodine scrub [Covetrus 11695-2217-1]
- Scalpel [Excel 29550]
- 70% ethanol wipes (for sterilization) [Covidien 6818]
- Sutures [Ethilon 669H)
- Eye lubricant (to prevent drying during anesthesia) [Dechra 17033-211-38]
- Insulin syringes (e.g., 31G) [BD 328290]
- Analgesics (e.g.,Nocita^{TM}:bupivacaine) [Elanco YL103060A]

Intravenous Injection

- Anesthesia induction chamber [Patterson Scientific 78933387]

- Anesthesia system (e.g., isoflurane vaporizer) [Matrx 94805059]
- Mouse/rat nose cone and tubing for anesthesia delivery
- Oxygen tank [Airgas Healthcare UN1072]
- Oxygen pressure regulator [Western Medica 96-M2-540-P]
- Isoflurane [Piramal 66794-017-25]
- 70% ethanol wipes [Covidien 6818]
- Eye lubricant [Dechra 17033-211-38]
- Surgical drapes [Dynarex 4410]
- Sterile saline (for flushing if needed)
- Heat source (lamp or warm water) for tail vein dilation
- Diluted chlorhexidine solution for tail sterilization
- Insulin syringes (e.g., 31G) [BD 328290]
- 25G–30G needles for mice [BD 305125, 305115, 305109, 305106]
- 22G–25G for rats [305156, 305145, 305125]
- 1 mL syringes [BD 309659]
- Occlusive device or manual pressure for vein visualization

Intra-Cisterna Magna Injection

- Ketamine/Xyzaline mixture for mice [Patterson, #07-894-8462 and 07-891-9200]
- 27-gauge needle to inject IP [BD 305109]
- 1 mL syringes [BD 309659]
- Stereotaxic frame [World Precision Instruments 505322]
- Mouse adaptor [Kopf Model 923-B]
- 27GX3/4”TW Scalp Vein Set [Extel 26709]
- Eye lubricant [Dechra 17033-211-38]
- 70% ethanol wipes [Covidien 6818]
- Scissors and forceps
- DecapiCones® [Braintree Scientific DC 200]
- CSF collection tubes (optional) [USA Scientific 1615-5500]
- Rat adaptor [Kopf Model 920]
- Rat anesthesia mask (Kopf Model 906)
- Anesthesia induction chamber [Patterson Scientific 78933387]
- Anesthesia system (e.g., isoflurane vaporizer) [Matrx 94805059
- Oxygen tank [Airgas Healthcare UN1072]
- Oxygen pressure regulator [Western Medica 96-M2-540-P
- Isoflurane [Piramal 66794-017-25]
- 30-gauge needle [BD 305106]

Intracerebroventricular Injection in Neonates

- Hamilton syringe (10 μL) with 30-gauge beveled needle [Hamilton 81022]
- Metal plate or glass dish (chilled on ice)
- Folded foil sheet for pup placement during anesthesia
- 70% ethanol wipes for skull sterilization [Covidien 6818]
- Nest material for scent familiarity during pup recovery
- Surgical drape [Dynarex 4410]

Retro-orbital injections

- Anesthesia induction chamber [Patterson Scientific 78933387]
- Anesthesia system (e.g., isoflurane vaporizer) [Matrx 94805059]
- Mouse/rat nose cone and tubing for anesthesia delivery
- Oxygen tank [Airgas Healthcare UN1072]
- Oxygen pressure regulator [Western Medica 96-M2-540-P]
- Isoflurane [Piramal 66794-017-25]
- Insulin syringes (31G) [BD 328290] or 25–27G needles [BD 305125, 305115, 305109]
- Topical ophthalmic analgesic (as per IACUC protocol)

Post-Injection Monitoring

- Recovery cage with soft bedding and heating pad placed under half of the cage floor
- Analgesics (e.g., buprehorphine)
- Scale (for weight monitoring)

Observation log sheets *Biosafety Requirements for AAV Injection*

- Compliance with institutional biosafety committees (IBC) requirements.

- Biohazard signage on cages and procedure rooms
- Proper ventilation and containment to prevent aerosol exposure.
- Autoclave bedding and cages for at least 72 hours post-injection.
- Use approved disinfectants (e.g., 0.5% sodium hypochlorite or 2% glutaraldehyde).
- Ethanol is not effective against AAV

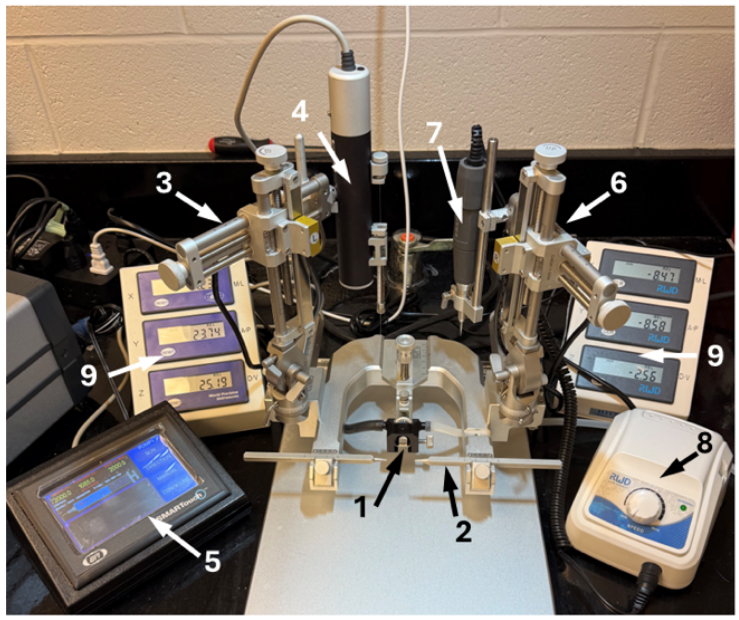

Figure 1. A typical surgical stereotaxic setup.
(1) Nose piece for positioning rodent's head with tubing delivering O2 and anesthesia. (2) Ear bars for holding rodent's head. (3) Stereotaxic left arm. (4) Syringe pump and syringe. (5) Pump controller for automated delivery. (6) Stereotaxic right arm. (7) Dremel drill. (8) Dremel controller. (9) Digital system attached to the stereotaxic arms for accurate needle and drill placement.

Methods

Intracranial Injections:

This protocol describes how to perform an aseptic stereotaxic survival surgery to deliver AAV vectors to the brain of a mouse.

Adult Rodents

All procedures presented here were approved by the University of South Florida Animal Care and Use Committee. Adjustments to meet specific institutional requirements might be necessary. Animals are first acclimated for 30 min in the surgery room to minimize stress. Then, the animal is weighed (weight is recorded for post op follow up) and placed in the anesthesia induction chamber with a calibrated vaporizer delivering isoflurane anesthetic. Induction with anesthesia is typically performed with a vaporizer flow rate of 3-5% with oxygenation at 0.5%. Once anesthesia is evident via pedal withdrawal reflex test, the fur on the top of the head, from the nape of the neck up into between the eyes and ears laterally, is trimmed to prevent contaminating the operative site; paw trimmers work excellent for mice and electric clippers work well on rats. The rodent is then placed on a surgical drape atop an isothermal pad within the surgical field and mounted into the stereotaxic apparatus. Figure 1 shows a typical set-up for rodent surgery (for mice and rats, the nose piece can be easily exchanged). To mount the animal into the frame, they are first placed in the nose cone with the top front teeth placed correctly in the cone. This allows maintenance of anesthesia at a flow rate of ~2% by surgical tubing attached to the rodent-specific nose cone apparatus (Figure 2A). Subsequently, ear bars or cuffs are used to position the head in a fixed stationary position for the surgery. Then, the shaved area of the head is wiped with a 70% alcohol pad. Approved preemptive analgesic is delivered prior to the incision. We prefer to use Nocita® as an approved analgesic, which is injected under the skin on the top of the head with a 31-gauge insulin syringe. This allows for long-lasting localized effects (72 hours), thus requiring less injections and less stress for the animals. The analgesic is administered subcutaneously in the skin above the skull, and at least 2 minutes are allowed to pass prior to incision. During this 2-minute period, the top of the head can be massaged to facilitate dispersion of the Nocita® and eye lubricant is applied to prevent dryness.

The skin on top of the head is then cleaned with germicidal surgical scrub (wiping from the center of the surgical field outward). The surgical site is painted with a dilute, tamed iodine solution. A sterile surgical drape material over the animal (such as Bioclusive) is used to maintain sterility within the surgical field.

Using a scalpel (#10 or #11), a single incision is made on the top of the skull. Two sterile surgical swabs are used to clean and dry the skull while moving the skin apart to sufficiently expose the skull (Figure 2B). Alternatively, the skin can be held open using two

mosquito hemostats clamped to the subcutaneous material. For targeted intracranial injections, stereotaxic coordinates are determined using a mouse brain atlas, which presents coronal or sagittal sections overlaid with a millimeter-scale grid. Coordinates are referenced from bregma, the intersection of the coronal and sagittal sutures, across three dimensions: the x-axis (anterior-posterior), y-axis (medial-lateral), and z-axis (depth) (Paxinos and Watson, 2013; Paxinos and Franklin, 2019). It is essential to verify that the skull is properly leveled within the stereotaxic frame. The microdrill attached to one stereotaxic arm can be used to confirm that the skull is level in both the X and Y planes. To confirm that the skull is level on the Y plane, position the drill bit slightly ahead of bregma, bring the drill bit down until it is just barely touching

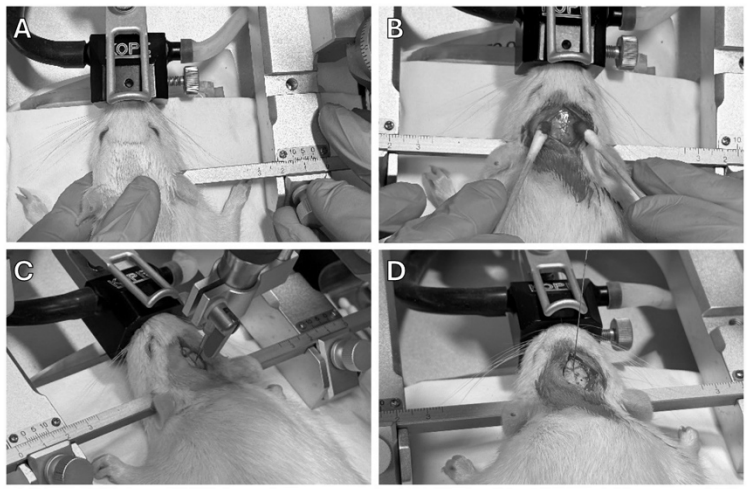

Figure 2. Stereotaxic intracranial injection in an adult rat.
(A) Positioning of rat in nose cone and placement of ear bars. (B) Cleaning and drying of the skull after incision. (C) Drilling of hole with Dremel in target area. (D). Positioning of syringe at bregma before guiding it to the injection site.

the skull, and zero out the Z coordinate. Bring the drill bit back up, position it slightly behind bregma, and then bring the drill bit down the same distance as before. The Z coordinate should be zero. The position of the nose can be adjusted up or down in the frame to adjust the skull to a level position, and the positioning checked again. Repeat this procedure to test that the skull is level on the X plane by moving the drill bit slightly to the left and then to the right of bregma. Bregma and Lamba could also be used as points of zero reference. The microdrill is then placed at bregma, and the coordinates are zeroed out. Afterwards, the microdrill is then moved under stereotaxic guidance to the region of interest, and the hole is drilled through the skull (Figure 2C). Multiple drill holes can be performed, e.g. one may target the hippocampus and anterior cortex within one animal. A hand-held microdrill may be used if the stereotaxic equipment does not have a separate arm for the drill attachment. In this case, the needle would be used to identify the stereotaxic coordinates from bregma for correct hole placement.

Performing pilot injections may be of value to ensure correct targeting. This could be performed with a dye or ink, immediately followed by gross brain sectioning to identify correct injection placement. Examples of routinely used coordinates within our laboratory for adult mice and rats are indicated in Table 1. Coordinates will need to be adjusted for smaller or younger animals.

Mouse	Lateral (X)	Anterior-Posterior (Y)	Dorsal-Ventral (Z)
Hippocampus	±2.7	-2.7	-3.0
Anterior cortex	±2.0	+2.0	-2.0
Substantia nigra	±1.4	-2.8	-4.6
Lateral Ventricle	±1.0	-0.4	-2.4
Cerebellum	±1.7	-6.4	-3.7
Rat	Lateral (X)	Anterior-Posterior (Y)	Dorsal-Ventral (Z)
Hippocampus	±4.6	-6.0	-5.0
Substantia nigra	±2.0	-5.2	-8.2
Lateral Ventricle	±1.5	-0.5	-4.3
Thalamus	±2.7	-3.3	-6.3

Table 1: Stereotaxic coordinates of adult rodents from bregma for viral injections to commonly targeted brain regions used in our laboratory.

A Hamilton syringe is placed in the injector on the opposite stereotaxic arm and the needle point is moved to bregma to zero out the coordinates (Figure 2D). The needle is then moved to the desired anatomical coordinates for injection. For parenchymal injections 2 μL of viral vector are dispensed per site at a flow rate of 2.5 μL/min using convection enhanced delivery (CED). We have published using bilateral injections in the hippocampus and anterior cortex and published sustained expression in both rats and mice models (Carty et al., 2013; Joly-Amado et al., 2020;

Nenninger et al., 2022). CED injections can be reviewed here (Nash and Gordon, 2016). A timer set to 2 min is started concomitantly with the injection, allowing the needle to be kept in position for one minute. This reduces the chance of back flow and allow complete dispersion of the virus. Longer times can be used to leave the needle in place and other typical viral injections have been reported with flow rates of 0.5 µL/min (Cearley et al., 2008; Jaworski et al., 2009).

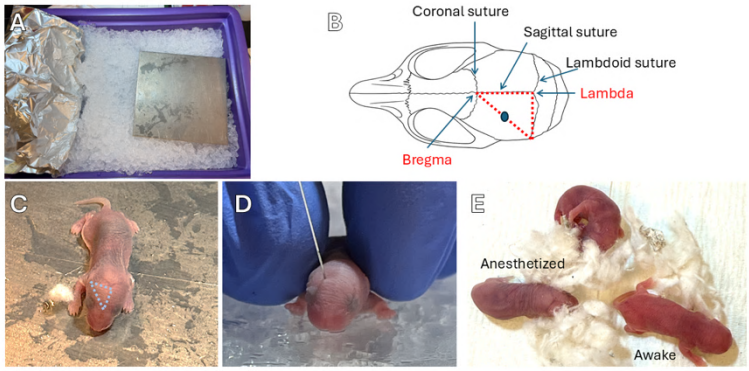

Figure 3. Intracerebroventricular injection into mouse neonates.
(A) Foil and metal plate setup on ice. (B) Diagram of targeted injection site. (C) Overlay of targeted injection site in a pup. Note the color of the pup is indicative of anesthesia. (D) Injection into skull with syringe. (E) Phenotypical comparison of blueish anesthetized versus pink awake pups.

After injection (single or multiple), the incision is closed with nylon (Ethilon® or an equivalent product) sutures. The rodent is placed into a clean home cage with at least half of the cage on an isothermal/warming pad. The animals are monitored until recovery (typically within 10-20 min), with the time of induction and wakefulness recorded.

Intracerebroventricular Injection into Postnatal Day 0 (P0) Pups

On ice, place a metal plate or glass dish along with a folded piece of foil (Figure 3A). Prepare a warming pad for recovery after the injections. Load a Hamilton syringe (10 µL) with a 30-gauge beveled needle with the desired amount of AAV for injection (2 µL of viral vector per lateral ventricle).

The mother can be removed to another cage to limit her exposure to the removal of the pups. Alternatively, half of the pups can be removed from the mother first, so that she remains associated with some pups at all times. P0 pups are placed in the foil on ice to induce anesthesia. After a few minutes (no more than five minutes), the pups will begin to show a purple-bluish hue and become inactive, which indicates they are anesthetized. A pup is then moved from the foil onto the metal/glass plate. This step is also performed on ice to maintain anesthesia during injection. The top of the head is gently swabbed with a 70% alcohol wipe. The suture lines of the skull should be clear. Forming a right-angled triangle from bregma to lambda to the intersection of the parietal-interparietal and interparietal-occipital sutures, find the midpoint along the hypotenuse to perform the injection (Figures 3B and 3C). The needle is depressed through the skull 2 millimeters (Figure 3D). A 2 millimeter mark can be made on the needle so as not to depress too deeply into the brain. The AAV solution is injected slowly and consistently. Once everything has been dispensed, the needle is left in place for approximately 10 seconds prior to removal. This process is repeated on the contralateral side.

The pup is then immediately placed on the warming pad to restore its body temperature. A small amount of nest material can be placed with the pup so that it has a familiar scent around it. Once the pink color returns and the mouse is warm and active, it can be placed back into the home cage (Figure 3E). Observe mother to ensure care of the pups is continued and she is not rejecting them. In the past we have occasionally attempted to use foster moms when animals do not seem to take care of their offspring, but unless there is a relatively large breeding colony this may not be feasible for most labs.

Intravenous Injections in Adult Rodents:

Tail Vein

Tail vein injections are the primary method of performing intravenous injections in rodents. To start, the animal is placed in an anesthesia induction chamber which delivers a 3-5% flow rate of isoflurane with 0.5% oxygenation. Following successful pedal withdrawal reflex test to verify the animal has been anesthetized, it is placed atop a surgical drape on a warming/isothermal pad and attached to an appropriate nose cone for sustained delivery of anesthesia during injection (Figure 4A). Lubricant

may be placed on the eyes, so they do not dry out during injection. To make the vein more visible, the animal's tail is warmed. This can be performed with a heat lamp or using warm water (a damp paper towel soaked in warm water can be used). The appropriate needle size for tail vein injections is 25G-30G and 22G-25G for mice and rats, respectively.

Figure 4. Intravenous tail and retro-orbital injections in a rat.
(A) Maintenance of anesthesia with a nose cone. (B) Injection into the tail vein. (C) Restraint of rat's head to shift eyeball out of the socket. (D) Injection into the medial canthus to access the retro-orbital sinus.

Preceding injection, the tail is sterilized with 70% ethanol wipes. For rats, scrubbing with chlorohexidine prior to sterilization may help remove some of the sebum accumulated as they age. When the tail has been sufficiently cleaned and sterilized, apply occlusive pressure above the intended injection site to aid in visualization of the tail vein. Once ready for injection, puncture the vein and draw back the syringe. The appearance of a blood flash in the syringe indicates successful entry into the vein. Upon confirmed access to the vein, slowly inject the viral solution, applying consistent pressure (Figure 4B). Successful injection is indicated by the vein clearing upon virus administration. Standard injection volumes do not exceed 200 µL in mice and 500 µL in rats.

Retro-orbital injection in adult rodent

Retro-orbital injections are an alternative to intravenous tail injections. It is recommended that no more than 6 injections (3 per eye) be administered within a rodent's lifespan. Injection volumes should be limited to 0.1 to 0.3 mL. Start by placing the rodent in an anesthesia induction chamber delivering isoflurane at a flow rate of 3-5% with oxygenation at 0.5%. Isoflurane is preferred for fast recovery. Once the rodent is anesthetized, as indicated by pedal withdrawal reflex test, it is removed from the chamber and attached to a nose cone delivering isoflurane at a flow rate of 2-3% with oxygenation at 0.5%. The anesthetized rodent should be placed laterally on a surgical drape on top of an isothermal pad (Figure 4A).

Using the forefinger and thumb, obtain a secure hold of the forehead and jaw, applying pressure on the head to make the eyeball pop out from the eye socket (Figure 4C). Care should be taken to not overexert pressure on the trachea, as breathing can be interrupted and/or collapse of the trachea can occur. With the other hand, insert the needle straight down into the medial canthus, with the bevel facing away from the eye (Figure 4D). A 31-gauge insulin syringes is preferred, but 25-27 gauge needles are also appropriate. Ensure that even and consistent pressure is applied onto the head and jaw to prevent the eyeball from sinking back down into the socket. Continue moving the needle downwards until the bone at the back of the eye is felt. When the needle is fully in the retro-orbital sinus, the full volume of the syringe is dispensed. Avoid pushing down or applying pressure with the needle, as this may lead the retro-orbital sinus to be punctured or ruptured. This may cause the injected material to leak from the nasal cavity, in which case veterinary assistance should be sought immediately. Proper injection will result in a visible bulging or blanching of the eye, with no leakage or bleeding. Once the full volume has been dispensed, move the needle backwards out of the medial canthus and swiftly use the fingers that were holding the jaw and forehead to roll the eyelids over the eyeball, situating it back into the eye socket. After the injection is complete, the rodent should be returned to a clean cage for recovery, with movement returning in less than a minute.

Lubricant can be placed onto the eye to prevent the cornea from drying out. A topical ophthalmic analgesic can be administered as per the institution's IACUC protocol. If the eye appears ruptured, damaged, or excessively dry during or after the injection, the institution's veterinarian should be

promptly consulted to ensure appropriate care for the rodent.

Intra-Cisterna Magna Injection in Adult Rodents:

Intra-cisterna magna (ICM) injections allow for injection of virus directly into the cerebrospinal fluid (CSF), allowing for delivery of the viral vector throughout the central nervous system (Figure 5A). This is considered a less invasive administration route compared to direct injection into the lateral ventricles.

Adult Mice

To begin, a 27GX3/4"TW Scalp Vein Set attached to a 1mL syringe will be needed. The scalp vein (butterfly) needle is attached to the arm of the stereotaxic instrument. Slight bending of the needle will occur. Position the ear bars on the equipment so that they are equal in distance (symmetrical) and the ends of the ear bars are touching. Position the needle until it is directly above where the ear bars meet and then zero out the X/Y coordinates (Figure 5B). This establishes the X coordinate on the midline of the mouse skull.

Inject the mouse with a Ketamine/Xylazine mixture (1.75 mL Ketamine (100mg/mL), 0.25 mL Xylazine (100mg/mL), 8 mL saline) at a dose of 0.1mL/20g intraperitoneally. Once the mouse is anesthetized, shave the top of the head down to the neck. Place the mouse on a heating pad and insert the ear bars symmetrically (Figure 5C). Clean the shaved area of the head with an ethanol wipe and apply lubricant to the eyes.

Tilt the head forward (70°) over the edge of the heating pad. Brace the mouthpiece against the forehead (Figure 5D). Use a finger to feel for the soft tissue directly below the occipital protuberance of the skull. Adjust the position of the needle in the Y axis until it is touching the very top of the skin below the occipital protuberance (Figure 5E). The Z coordinate can be zeroed out for reference. Begin to slowly lower the stereotaxic arm with the needle attached. As the needle enters the skin, there should be no resistance or shifting of the skull. Continue to lower the needle through the tissue, while simultaneously gently pulling back on the 1 mL syringe. This will allow for identification of the presence of CSF and allow for CSF sampling (Figure 5F). We observed that the depth of Z coordinate where we obtained CSF ranged from 2-5 mm. Once CSF is observed in the tubing of the needle, halt the descent of the needle. Clamp the tubing using forceps, leaving a small gap for injections (Figure 5G). Cut the tubing directly above the clamped forceps and immediately place the collected CSF in a tube on ice. To deliver the virus, insert the needle into the tubing, below where the forceps are clamped, and slowly dispense the desired volume of treatment, which should be no greater than 10 μL (Figure 5H). Wait 1 minute after all the virus has been dispensed, then unclamp the forceps

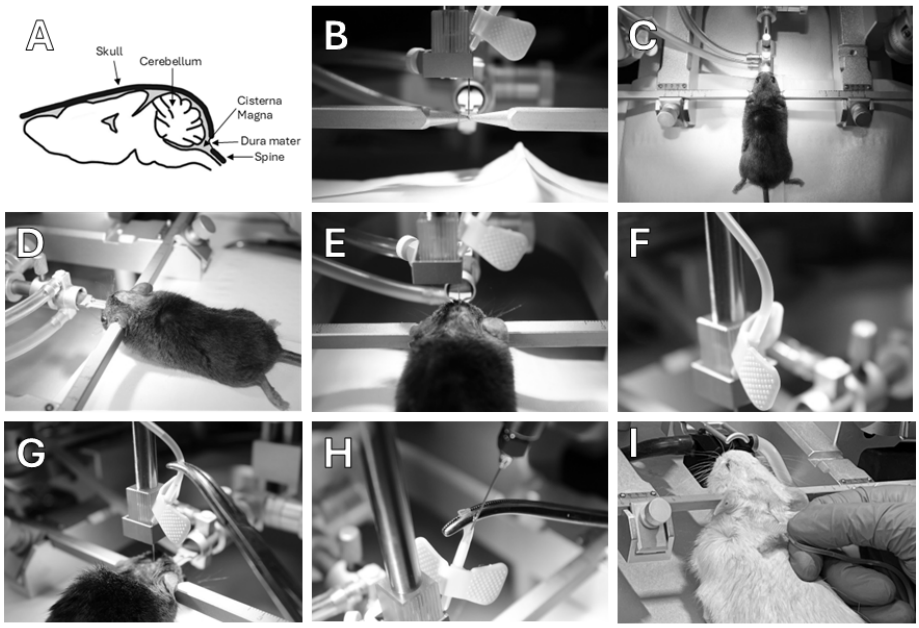

Figure 5. Procedural steps of intra-cisterna magna injections in rodents.
(A) Diagram of where the cisterna magna is located. (B) Positioning of needle where ear bars meet so that the X/Y coordinates can be zeroed out. (C) Adult mouse situated into stereotaxic apparatus with ear bars inserted. (D) Mouthpiece of the stereotaxic equipment pushed up against the forehead of the mouse. (E) Needle tip touching the top of the tissue below the occipital protuberance. (F) CSF flowing through the tubing. (G) Clamping of the tube directly below where the CSF collected. (H) The tubing is cut above where it is clamped and the syringe with the virus is inserted into the tubing below the clamping. (I) Adult rat with a butterfly needle inserted into the cisterna magna for CSF collection.

and allow the solution to flow down into the cisterna magna. Wait an additional 2 minutes after unclamping the forceps. To further enhance delivery, mice can be placed in the Trendelenburg position. We have placed mice in DecapiCones® at 30° decline on top of a heating pad (the cone has an open end for easy breathing but gives support to the animal, holding it steady in a decline).

Adult Rats

In rats, we can take a different approach because of their larger size. A rat can be anesthetized with a vaporizer flow rate of 3-5% with oxygenation at 0.5%. Once anesthesia is evident, the fur from the top of the head and down the neck is shaved. The anesthetized rat is placed in the stereotaxic frame on top of a surgical drape and heating pad. Insert the ear bars symmetrically and disinfect the shaved area with an ethanol wipe. Remove the heating pad from below the animal so that the body is now lower than the head, allowing the neck to be exposed in a more vertical position (Figure 5I). Using the index finger of the hand not doing the injection (typically nondominant), feel for the soft tissue directly below the occipital protuberance of the skull. Using a fingernail as a guide, position the 30 gauges needle on top of the fingernail and under the occipital protuberance, then penetrate through the skin (Figure 5I). There should be a resistance as the needle passes through the dura mater into the cisterna magna space. Then, withdraw the syringe to observe CSF and inject the virus. If a hard surface is encountered while attempting to pass through the dura, indicating contact with the skull, reposition the needle at a lower angle and proceed through the dura mater. We administer 20 μL of virus sample, but a typical range of 10-50 μL has been reported for CSF injections in rats. This technique can be used for mice but due to their significantly smaller size, it is difficult to complete freehand, so we have used the method described above. We do however use this technique in mice when we sample CSF. Using 27GX3/4”TW Scalp Vein Set attached to a 1mL syringe as above, the needle can be positioned into the cisterna magna and the syringe gently withdrawn. If it is a terminal procedure, we can obtain ~200 μL of clean CSF with this method.

Summary

Direct intracranial injections, while inherently invasive, offer a significant advantage: precise targeting of specific brain regions. In our studies, targeted delivery to areas such as the hippocampus (Carty et al., 2010), anterior cortex (Joly-Amado et al., 2020) and substantia nigra (Nash et al., 2015) has consistently resulted in robust and widespread distribution of viral vectors within these regions. Conversely, intracerebroventricular injections using AAV serotypes such as 9 or 10 have proven highly effective for achieving broad, global transduction across the central nervous system, making them a powerful tool for systemic gene delivery (Finneran et al., 2019).

P0 intracranial injections of rAAV offer several compelling advantages for gene delivery to the brain. At this early developmental stage, the blood-brain barrier is still immature, allowing rAAV vectors to cross more readily and achieve widespread distribution throughout the central nervous system. This results in efficient transduction of both neurons and glial cells across various brain regions. The procedure is minimally invasive compared to intracranial injections, reducing surgical risks and making it particularly suitable for early-life interventions. Additionally, the neonatal immune system is less reactive, which may lower the likelihood of immune responses against the viral vector, enhancing safety and long-term transgene expression. Administering gene therapy at P0 also enables early correction of genetic disorders, potentially preventing the onset or progression of neurological diseases. Some examples from our work and that of others can be found here (Chakrabarty et al., 2013; Cook et al., 2015; Carlomagno et al., 2019).

Recent developments in capsid engineering by directed evolution have led to the creation of rAAV variants that can cross the blood-brain barrier more efficiently than standard AAV serotypes administered intravenously. This has opened this route of administration for rAAV gene delivery to the brain. Such vectors include PhP.eB and CAP-B22, which were derived from the original AAV9 serotype (Chan et al., 2017; Goertsen et al., 2022). These vectors can achieve wide spread brain transduction (Finneran et

al., 2024), but currently do not target all neurons. Another limitation to these vectors is the requirement for a larger amount of virus to be injected to achieve significant brain transduction, however, improvements in vector design continue in the field.

Intracisternal injections offer a potentially minimally invasive and effective route for delivering rAAV vectors directly into the CSF of rodents. It has been proposed that this method enables widespread distribution of the viral vector throughout the central nervous system via CSF flow, facilitating transduction of brain and spinal cord tissues (Bailey et al., 2020; Chatterjee et al., 2022). However, some studies report that cisterna magna injections can lead to limited transduction efficiency in certain brain regions due to restricted CSF flow or anatomical barriers (Ye et al., 2024). Perhaps transduction efficiency differences between studies may depend on the AAV serotype, dose, and infusion parameters. This method has been shown to be effective in large animal models which does suggest a potential translatability to human applications (Taghian et al., 2020; Nakamura et al., 2021; Hunter et al., 2025). The Trendelenburg position, where the animal is placed with its head lower than its body, has been proposed to offer several benefits during cisterna magna injections. Trendelenburg positioning after injection has been shown to enhance virus transduction to the brain and spinal cord (Castle et al., 2018; Chatterjee et al., 2022). However, the amount of time inclined and the species of animal may contribute to the effectiveness of this method.

References

Bailey RM, Rozenberg A, Gray SJ (2020) Comparison of high-dose intracisterna magna and lumbar puncture intrathecal delivery of AAV9 in mice to treat neuropathies. Brain Res 1739:146832.

Carlomagno Y, Chung DC, Yue M, Kurti A, Avendano NM, Castanedes-Casey M, Hinkle KM, Jansen-West K, Daughrity LM, Tong J, Phillips V, Rademakers R, DeTure M, Fryer JD, Dickson DW, Petrucelli L, Cook C (2019) Enhanced phosphorylation of T153 in soluble tau is a defining biochemical feature of the A152T tau risk variant. Acta Neuropathol Commun 7:10.

Carty N, Lee D, Dickey C, Ceballos-Diaz C, Jansen-West K, Golde TE, Gordon MN, Morgan D, Nash K (2010) Convection-enhanced delivery and systemic mannitol increase gene product distribution of AAV vectors 5, 8, and 9 and increase gene product in the adult mouse brain. J Neurosci Methods 194:144-153.

Carty N, Nash KR, Brownlow M, Cruite D, Wilcock D, Selenica ML, Lee DC, Gordon MN, Morgan D (2013) Intracranial injection of AAV expressing NEP but not IDE reduces amyloid pathology in APP+PS1 transgenic mice. PloS one 8:e59626.

Castle MJ, Cheng Y, Asokan A, Tuszynski MH (2018) Physical positioning markedly enhances brain transduction after intrathecal AAV9 infusion. Sci Adv 4:eaau9859.

Cearley CN, Vandenberghe LH, Parente MK, Carnish ER, Wilson JM, Wolfe JH (2008) Expanded repertoire of AAV vector serotypes mediate unique patterns of transduction in mouse brain. Mol Ther 16:1710-1718.

Chakrabarty P, Rosario A, Cruz P, Siemienski Z, Ceballos-Diaz C, Crosby K, Jansen K, Borchelt DR, Kim JY, Jankowsky JL, Golde TE, Levites Y (2013) Capsid serotype and timing of injection determines AAV transduction in the neonatal mice brain. PloS one 8:e67680.

Chan KY, Jang MJ, Yoo BB, Greenbaum A, Ravi N, Wu WL, Sanchez-Guardado L, Lois C, Mazmanian SK, Deverman BE, Gradinaru V (2017) Engineered AAVs for efficient noninvasive gene delivery to the central and peripheral nervous systems. Nat Neurosci 20:1172-1179.

Chatterjee D, Marmion DJ, McBride JL, Manfredsson FP, Butler D, Messer A, Kordower JH (2022) Enhanced CNS transduction from AAV.PHP.eB infusion into the cisterna magna of older adult rats compared to AAV9. Gene Ther 29:390-397.

Cook C, Kang SS, Carlomagno Y, Lin WL, Yue M, Kurti A, Shinohara M, Jansen-West K, Perkerson E, Castanedes-Casey M, Rousseau L, Phillips V, Bu G, Dickson DW, Petrucelli L, Fryer JD (2015) Tau deposition drives neuropathological, inflammatory and behavioral abnormalities independently of neuronal loss in a novel mouse model. Hum Mol Genet 24:6198-6212.

Finneran DJ, Morgan D, Gordon MN, Nash KR (2019) CNS-Wide over Expression of Fractalkine Improves Cognitive Functioning in a Tauopathy Model. J Neuroimmune Pharmacol 14:312-325.

Finneran DJ, Desjarlais T, Henry A, Jackman BM, Gordon MN, Morgan D (2024) Induction of tauopathy in a mouse model of amyloidosis using intravenous administration of adeno-associated virus vectors expressing human P301L tau. Alzheimers Dement (N Y) 10:e12470.

Goertsen D, Flytzanis NC, Goeden N, Chuapoco MR, Cummins A, Chen Y, Fan Y, Zhang Q, Sharma J, Duan Y, Wang L, Feng G, Chen Y, Ip NY, Pickel J, Gradinaru V (2022) AAV capsid variants with brain-wide transgene expression and decreased liver targeting after intravenous delivery in mouse and marmoset. Nat Neurosci 25:106-115.

Gorzek RC, Joly-Amado A, Hurst-Calle N, Gabrielson GL, Miller M, Osting S, Nash KR, Burger C (2025) Adeno-Associated Viral Gene Delivery of Wild-Type Human Tau Induces Progressive Hyperphosphorylation and Neuronal Cell Death in the Hippocampi of Middle-Aged Rats. Cells 14.

Hunter JE, Vite CH, Molony CM, O'Donnell PA, Wolfe JH (2025) Intracisternal vs intraventricular injection of AAV1 result in comparable, widespread transduction of the dog brain. Gene Ther 32:184-188.

Ideno J, Mizukami H, Honda K, Okada T, Hanazono Y, Kume A, Saito T, Ishibashi S, Ozawa K (2003) Persistent phenotypic correction of central diabetes insipidus using adeno-associated virus vector expressing arginine-vasopressin in Brattleboro rats. Mol Ther 8:895-902.

Jaworski T, Dewachter I, Lechat B, Croes S, Termont A, Demedts D, Borghgraef P, Devijver H, Filipkowski RK, Kaczmarek L, Kugler S, Van Leuven F (2009) AAV-tau mediates pyramidal neurodegeneration by cell-cycle re-entry without neurofibrillary tangle formation in wild-type mice. PloS one 4:e7280.

Joly-Amado A, Hunter J, Quadri Z, Zamudio F, Rocha-Rangel PV, Chan D, Kesarwani A, Nash K, Lee DC, Morgan D, Gordon MN, Selenica MB (2020) CCL2 Overexpression in the Brain Promotes Glial Activation and Accelerates Tau Pathology in a Mouse Model of Tauopathy. Front Immunol 11:997.

Leroy BP, Fischer MD, Flannery JG, MacLaren RE, Dalkara D, Scholl HPN, Chung DC, Spera C, Viriato D, Banhazi J (2023) Gene Therapy for Inherited Retinal Disease: Long-Term Durability of Effect. Ophthalmic Res 66:179-196.

Ling Q, Herstine JA, Bradbury A, Gray SJ (2023) AAV-based in vivo gene therapy for neurological disorders. Nat Rev Drug Discov 22:789-806.

Matuszek Z, Brown BL, Yrigollen CM, Keiser MS, Davidson BL (2025) Current trends in gene therapy to treat inherited disorders of the brain. Mol Ther 33:1988-2014.

Nakamura S, Osaka H, Muramatsu SI, Takino N, Ito M, Jimbo EF, Watanabe C, Hishikawa S, Nakajima T, Yamagata T (2021) Intra-cisterna magna delivery of an AAV vector with the GLUT1 promoter in a pig recapitulates the physiological expression of SLC2A1. Gene Ther 28:329-338.

Nash KR, Gordon MN (2016) Convection Enhanced Delivery of Recombinant Adeno-associated Virus into the Mouse Brain. Methods Mol Biol 1382:285-295.

Nash KR, Moran P, Finneran DJ, Hudson C, Robinson J, Morgan D, Bickford PC (2015) Fractalkine over expression suppresses alpha-synuclein-mediated neurodegeneration. Mol Ther 23:17-23.

Nenninger AW, Willman M, Willman J, Stewart E, Mesidor P, Novoa M, Morrill NK, Alvarez L, Joly-Amado A, Peters MM, Gulick D, Nash KR (2022) Improving Gene Therapy for Angelman Syndrome with Secreted Human UBE3A. Neurotherapeutics 19:1329-1339.

Paxinos G, Watson C (2013) The Rat Brain in Stereotaxic Coordinates, 7th Edition Edition: Elsevier Science.

Paxinos G, Franklin KBJ (2019) The Mouse Brain in Stereotaxic Coordinates, 5th Edition Edition: Elsevier Science.

Rivera VM, Gao GP, Grant RL, Schnell MA, Zoltick PW, Rozamus LW, Clackson T, Wilson JM (2005) Long-term pharmacologically regulated expression of erythropoietin in primates following AAV-mediated gene transfer. Blood 105:1424-1430.

Taghian T et al. (2020) A Safe and Reliable Technique for CNS Delivery of AAV Vectors in the Cisterna Magna. Mol Ther 28:411-421.

Wang S, Xiao L (2025) Progress in AAV-Mediated In Vivo Gene Therapy and Its Applications in Central Nervous System Diseases. Int J Mol Sci 26.

Ye D, Chukwu C, Yang Y, Hu Z, Chen H (2024) Adeno-associated virus vector delivery to the brain: Technology advancements and clinical applications. Adv Drug Deliv Rev 211:115363.

fast DART
DATA, ANALYSIS, REVIEWS, TECHNIQUES E-JOURNAL

Biotechniques

Standardized Electrophysiological Approaches for CA1 Field Recordings: Insights into the AS Mouse Model

Melinda M Peters [1], Joseph E. Pick [2] and Edwin J. Weeber [3*]

[1]Independent Researcher, PA, USA
[2]Independent Researcher, NY, USA
[3]Foundation for Angelman Syndrome Therapeutics, San Antonio, TX, USA
[*]Corresponding author; edwin.weeber@cureangelman.org

Article History
Submitted: September 18, 2025 Accepted: October 24, 2025 Published: November 1, 2025

Abstract

The hippocampal CA3/CA1 Schaffer collateral pathway provides a lamina-resolved and highly reproducible synaptic pathway for quantifying synaptic transmission and plasticity in acute rodent brain slices. This paper consolidates best practices for CA1 field electrophysiology and links them to disease-relevant readouts in Angelman syndrome (AS) models. We detail a rigorously controlled pipeline spanning sucrose-based, low-Ca^{2+}/high-Mg^{2+} cutting solutions; staged recovery from ice-cold to warmed (30–32 °C) artificial cerebrospinal fluid (ACSF); strict management of bicarbonate buffering to prevent divalent precipitation; and recording parameters that yield clean, minimally filtered field excitatory post-synaptic potentials (EPSPs). Quantification emphasizes the initial field excitatory post-synaptic potential (fEPSP) slope measured within a fixed, pre-registered window, normalization to a stable baseline, and exclusion criteria that guard against artifacts. We outline how input–output curves, establish basal synaptic gain and the operating point for plasticity assays, and we compare induction paradigms-consisting of classical 100 Hz high frequency stimulation (HFS), theta-frequency and theta-burst stimulation, and ultra-high-frequency stimulation. Applying this framework to AS mouse and rat models, we summarize how electrophysiology discriminates a shifted induction threshold from a true capacity deficit requiring restoration of downstream expression mechanisms or Ube3a function. The approach delivers a mechanistically interpretable, quantitative biomarker for AS that is suitable for preclinical screening and for testing gene-targeted and synaptic-level therapies. Collectively, these standardized practices, spanning anatomy, solutions, data acquisition, and analysis, establish a reproducible framework and a translational lens for interpreting hippocampal LTP in AS and other neurodevelopmental disease models.

Keywords: Long-term potentiation, hippocampus, high frequency stimulation, animal models, synapse, synaptic function, synaptic plasticity.

Introduction

The hippocampal formation (dentate gyrus-CA3-CA1-subiculum) is both anatomically simple and exquisitely ordered, which is why it has been a standard of synaptic physiology for decades. Entorhinal cortex layer II neurons project via the perforant path to the dentate gyrus (DG), whose granule cells send mossy fibers to CA3 (terminating in

stratum lucidum) (Witter, 2007) (Amaral et al., 2007). CA3 pyramidal neurons then project to CA1 via the Schaffer collaterals (SCs), while a parallel "temporoammonic" input from entorhinal layer III reaches the distal apical tufts of CA1 in stratum lacunosum-moleculare (Remondes and Schuman, 2002). CA1 outputs to the subiculum and back to entorhinal cortex, completing the hippocampal–entorhinal loop that supports episodic/declarative memory and spatial navigation (OKeefe and

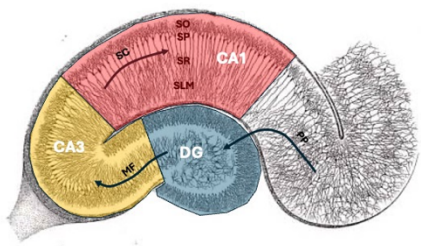

Figure 1. Organization of the hippocampal formation in a transverse slice.
The schematic shows major subfields and laminae of the hippocampus, including the dentate gyrus (DG), CA3, and CA! regions. Entorhinal cortex layer II neurons project via the perforant path (PP) to granule cells of the DG, which in turn send mossy fiber (MF) projections to CA3 pyramidal neurons. CA3 neurons project to CA1 pyramidal neurons through the Schaffer collaterals (SCs). Within CA1, distinct laminae are indicated: stratum oriens (SO), stratum pyramidale (SP), stratum radiatum (SR), and stratum lacunosum-moleculare (SLM). Together, these structures comprise the canonical tri-synaptic circuit that supports hippocampal processing.

Dostrovsky, 1971; Eichenbaum, 2017).

A key advantage for physiology is the laminar architecture of the hippocampus, which separates cell bodies, dendrites, and axons into highly organized layers: in CA1, stratum oriens (basal dendrites/ interneurons), stratum pyramidale (pyramidal somata), stratum radiatum (proximal apical dendrites and Schaffer collateral terminals), and stratum lacunosum-moleculare (distal apical tufts receiving temporo-ammonic input) (Megias et al., 2001; Spruston, 2008). This lamination preserves afferent/efferent geometry in slices, minimizes pathway mixing, and creates distinct current source sink patterns so that extracellular signals map cleanly onto underlying synaptic events (Eccles, 1979; Payne et al., 1982; Viana Di Prisco, 1984). In practice, it allows one to place a stimulating electrode squarely in the SC axon bundle and a recording electrode in stratum radiatum a few hundred microns away to capture a large, monotonic population fEPSP with minimal contamination from other pathways (Schwartzkroin and Wester, 1975). Because SC terminals are densely packed along proximal CA1 apical dendrites, one gets an excellent signal-to-noise ratio and a wide dynamic range that is ideal for measuring changes in initial slope, input–output curves, paired-pulse facilitation, and plasticity (Manabe et al., 1993).

The SC-CA1 synaptic pathway is mechanistically convenient, as its long-term potentiation (LTP) is classically N-methyl-D-aspartate receptor (NMDAR) -dependent and largely postsynaptic, allowing for direct analysis of dendritic Ca^{2+} influx, CaMKII/ PKA/ERK signaling, alpha-amino-3-hydroxy-5-methyl isoxazolepropronic acid receptor (AMPAR) trafficking, and spine-level expression mechanisms (Collingridge et al., 1983; Bliss and Collingridge, 1993; Malenka and Bear, 2004). That contrasts with DG-CA3 mossy-fiber LTP, which is strongly presynaptic and NMDAR independent, and is powerful but less aligned with the postsynaptic rules that dominate neocortical circuits (Zalutsky and Nicoll, 1990). In CA1, the clean separation of inputs by layer (SC in radiatum vs. temporoammonic in lacunosum-moleculare) allows pathway-specific stimulation and straightforward occlusion controls using two independent Schaffer inputs (Remondes and Schuman, 2002). If needed, CA3 can be removed surgically to reduce recurrent activity without disrupting the local SC termination zone, further stabilizing baseline transmission and LTP induction (Madison and Nicoll, 1984). Together, the hippocampus's ordered circuitry,

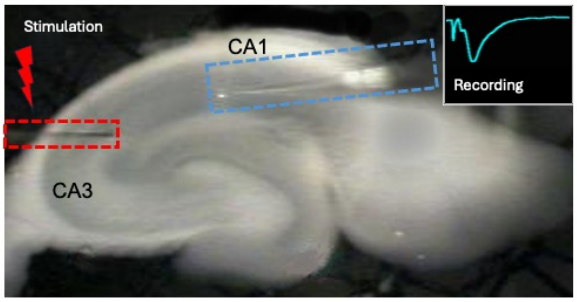

Figure 2. Photograph of a hippocampal slice positioned in an interface recording chamber.
An acute mouse hippocampal slice is shown resting on the porous membrane of the recording chamber, perfused with carbogenated ACSF at 30–32 °C. The bipolar stimulating electrode, indicated in the figure by a red dotted box, is positioned within the Schaffer collateral (SCs) pathway. The glass recording electrode (1–3 MΩ, ACSF-filled), indicated by a blue dotted box, is placed in the stratum radiatum (SR) of CA1 to capture field excitatory postsynaptic potentials (fEPSPs). A representative fEPSP trace is displayed, with the initial slope marked as the primary measure of synaptic efficacy. Strategic placement of stimulating and recording electrodes within CA1's laminar architecture enables robust, reproducible recordings with minimal pathway contamination, supporting input–output analyses, paired-pulse protocols, and long-term potentiation studies.

layered microanatomy, and the accessibility of the Schaffer collateral pathway make SC→CA1 the optimal choice for extracellular recordings of excitatory transmission and plasticity. One can stimulate a single, well-defined excitatory pathway, record a robust and lamina-locked fEPSP, and interpret changes in the initial slope as quantitative, pathway-specific shifts in synaptic strength, importantly, all with high reproducibility across slices, animals, and labs (Malenka and Bear, 2004).

Long-Term Potentiation

Long-term potentiation (LTP), first described in the 1970s, is the archetypal model for experience-dependent synaptic strengthening (Bliss and Lomo, 1973; Bliss and Richter-Levin, 1993). It refers to the persistent enhancement of synaptic efficacy following specific patterns of activity and is widely regarded as a cellular correlate of learning and memory (Malenka and Bear, 2004). The induction of LTP requires a cascade of tightly coordinated events, including presynaptic release of glutamate, postsynaptic activation of NMDA receptors, calcium entry into dendritic spines, and the engagement of intracellular signaling pathways such as CaMKII, PKA, and ERK/MAPK (Lisman et al., 2002; Sweatt, 2004). These molecular signals converge to alter AMPA receptor trafficking, modify the actin cytoskeleton, and drive gene transcription that stabilizes synaptic change (Kandel, 2001; Malinow and Malenka, 2002). In this way, LTP embodies the Hebbian principle of "cells that fire together wire together," providing a mechanistic bridge between activity patterns and enduring memory formation (Bi and Poo, 1998).

Electrophysiological field recordings in hippocampal slices have become the gold standard for studying LTP because they preserve much of the intrinsic connectivity of the circuit while permitting precise control over the extracellular environment. By recording fEPSPs in the stratum radiatum of CA1, investigators can quantify baseline synaptic strength, evaluate presynaptic release probability through paired-pulse paradigms, and induce LTP with defined stimulation protocols. This approach offers a reproducible and quantitative window into how synapses respond to activity, allowing researchers to parse contributions of specific receptors, signaling cascades, or pharmacological manipulations.

Importantly, field recordings also extend beyond basic mechanistic studies, providing a powerful translational platform for modeling human neurological and neurodevelopmental disorders (NDDs). In mouse models of human NDD and neurodegenerative disorders (ND), electro-physiological assays reveal characteristic synaptic phenotypes (Jiang et al., 1998; Palop et al., 2011). For example, shifts in input–output curves can signal diminished basal transmission, while abnormalities in paired-pulse facilitation may indicate presynaptic dysfunction (Manabe et al., 1993; Zucker and Regehr, 2002). Impaired LTP magnitude under specific induction paradigms can point to deficits in postsynaptic receptor signaling or downstream kinase pathways (Bliss and Collingridge, 1993; Malenka and Bear, 2004).

Thus, the study of hippocampal CA1 field electrophysiology provides dual benefits: it deepens our understanding of the cellular mechanisms underlying learning and memory while simultaneously offering insight into how genetic or molecular perturbations disrupt synaptic function in disease states. The following is a basic procedural guide for performing hippocampal CA1 electrophysiology and reviews examples of how this technique has provided insight into the molecular mechanism and consequences of Ube3a deficiency in various mouse models of AS.

Materials and Methods for LTP

Slice Preparation

Mice or rats are rapidly decapitated, potentially under deep anesthesia, and brains are immediately placed into ice-cold, carbogenated sucrose-based cutting solution. This solution is designed to minimize excitotoxicity during slicing by replacing most sodium with sucrose and by increasing Mg^{2+} and decreasing Ca^{2+} concentrations. A typical formulation used by Sweatt and colleagues contains (in mM): 110 sucrose, 60 NaCl, 3 KCl, 26 $NaHCO_3$, 1.25 NaH_2PO_4, 7 $MgCl_2$, 0.5 $CaCl_2$, 0.6 sodium ascorbate, and 10 glucose equilibrated with 95% O_2/5% CO_2 (Levenson et al., 2002; Weeber et al., 2003; Beffert et al., 2006; Moretti et al., 2006). Using a vibrating microtome (Leica VT1000 or equivalent vibrotome), 300–400 µm transverse hippocampal slices are prepared. The chosen thickness depends on the intended recording

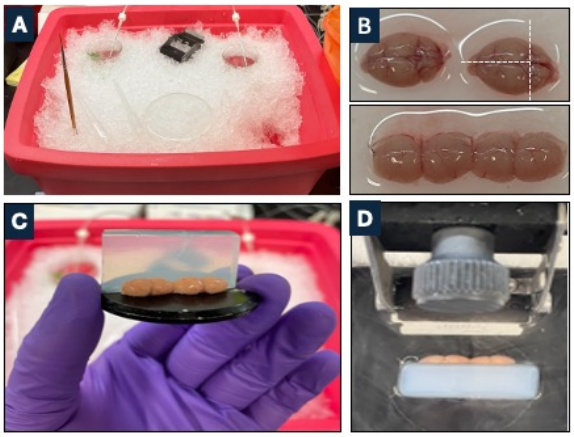

Figure 3. Preparation of acute hippocampal slices for electrophysiology.
(A) Ice bucket containing carbogenated cutting solution and transitional half cutting/half ACSF, maintained at near-ice temperature to preserve tissue viability during brain extraction and early handling. (B) Whole mouse brains immediately following dissection. The cerebellum is removed with a coronal cut just behind the inferior colliculi using a scalpel or iridectomy scissors. A sagittal cut is then made along the midline to separate the hemispheres. Each hemibrain is placed with the medial surface facing up, and the neocortex with the underlying hippocampus is separated from the midbrain and brainstem. Meninges and associated blood vessels are carefully removed to expose the hippocampus. (C) Positioning of the hemibrain on an agar block affixed to the slicing platform for stabilization during vibratome sectioning. (D) Hemibrain mounted on agar in the vibratome chamber immediately prior to slicing into 300-400 µm thick transverse sections. This stepwise preparation ensures preservation of hippocampal architecture for reliable electrophysiological recordings.

setup, as thinner slices (300 µm) are advantageous for whole-cell recordings in submersion chambers, whereas thicker slices (400 µm) are more applicable for field recordings in interface chambers (Hajos and Mody, 2009; Ting et al., 2014).

Brain Preparation

For acute slice electrophysiology, brains must be removed rapidly and with minimal disturbance to their intrinsic physiology. The standard approach is decapitation under brief isoflurane exposure or without prolonged anesthesia, followed by immediate immersion of the brain in ice-cold, carbogenated cutting solution (Ting et al., 2014). In contrast, systemic anesthesia can profoundly alter brain chemistry in ways that directly compromise electrophysiological measurements. Many anesthetics (e.g., pentobarbital, ketamine, urethane, or halothane) act on GABAA receptors, NMDA receptors, or potassium channels, which are the very targets under study in hippocampal synaptic physiology (Snyder et al., 2007; Speigel et al., 2023). Even a short exposure can change baseline excitability, suppress synaptic transmission, or modify intracellular signaling cascades such as MAPK and CaMKII. Residual drug bound to receptors in the tissue can persist after slicing, confounding results by reducing NMDA receptor responsiveness or enhancing inhibitory tone (Zorumski et al., 2016).

Moreover, anesthetics can alter neurotransmitter release, extracellular pH, and metabolic state, introducing variability in synaptic responses. For example, volatile anesthetics reduce glutamate release probability and depress hippocampal LTP induction, while barbiturates prolong inhibitory postsynaptic currents (Maclver et al., 1996; Zorumski et al., 2016). Because field electrophysiology assays rely on precise quantification of synaptic strength and plasticity, these drug-induced artifacts make it difficult to distinguish genuine disease phenotypes from anesthetic effects. Therefore, rapid decapitation, usually preceded only by minimal isoflurane to reduce distress, is the most reliable method to ensure that brain tissue reflects the animal's native physiology at the moment of euthanasia (Hajos and Mody, 2009; Ting et al., 2014). This approach preserves the integrity of synaptic currents, signaling pathways, and plasticity mechanisms, which are especially critical when comparing subtle differences between wild-type and disease model animals such as Angelman syndrome mice (Jiang et al., 1998).

ACSF Composition and Use

A precise, freshly prepared ACSF is essential for reliable fEPSP recordings because small shifts in divalent cations, pH, or osmolarity measurably change excitability, release probability, and plasticity thresholds (Hajos and Mody, 2009). ACSF needs to be prepared daily with 18 MΩ water and the exact recipe; continuously bubble with 95% O_2/5% CO_2 so the bicarbonate buffer sets pH 7.3–7.4 at the recording temperature (re-check pH after warming). To minimize loss of free Ca^{2+}/Mg^{2+} to insoluble salts, control order of addition and mixing: dissolve NaCl → KCl → glucose → $NaHCO_3$ → NaH_2PO_4 → $MgCl_2$ in ~80–90% final volume, continue carbogenation, and add $CaCl_2$ last after the solution clears and equilibrates. Avoid concentrated local contacts between $CaCl_2$ and bicarbonate or phosphate (common causes of $CaCO_3$ or $Ca_3(PO_4)_2$ precipitates); keep phosphate low (as in the recipe), maintain CO_2 in the reservoir with continuous oxygenation. Discard any solution that

turns hazy as "milky" ACSF means your free divalent levels are improper. When using drug additions, add from fresh stocks and keep vehicle (e.g., DMSO) ≤0.1% final. Be sure to protect light-sensitive antagonists (e.g., CNQX). For Mg^{2+}-free ACSF, replace $MgCl_2$ osmotically (e.g., with equimolar NaCl) and note the marked increase in network excitability. Consistency in formulation, order of addition, carbogenation, and same-day use prevents divalent precipitation and buffer drift, representing two silent failure modes that otherwise flatten slopes, shift LTP thresholds, and compromise reproducibility.

Recovery of Acute Hippocampal Slices

Recovery following slicing is a critical step in preparing acute hippocampal tissue for electrophysiological recordings. The slicing procedure itself is traumatic: axons and dendrites are severed, ionic gradients are disrupted, and cells experience transient depolarization. As a result, freshly cut slices are electrically silent and do not immediately display stable synaptic activity. A carefully staged recovery protocol is therefore essential to restore physiological function, re-establish ionic balance, and allow cells to regain excitability. The protocol typically begins with immersion of tissue in ice-cold cutting solution (Figure 3A), which reduces metabolic demand (Aghajanian et al., 1990). Importantly, cutting solution is formulated with low Ca^{2+} and high Mg^{2+} concentrations: low calcium minimizes activation of voltage-gated Ca^{2+} channels and excitatory neurotransmitter release during slicing, while high magnesium competitively blocks NMDA receptors. Together, these modifications suppress synaptic activity at the moment of tissue injury, protecting neurons from excitotoxic damage.

Once slices are sectioned, they are often transferred to a solution containing half cutting solution and half ACSF at near-ice temperature. This intermediate step allows a gradual transition between ionic environments and prevents sudden osmotic or ionic shock. Following this, slices are moved to room temperature ACSF (22–24 °C) for an extended recovery period, typically 60–90 minutes. During this phase, metabolic activity increases slightly, and neurons begin to re-establish resting potentials, synaptic vesicle cycling, and receptor function. At this stage, extracellular calcium is restored to

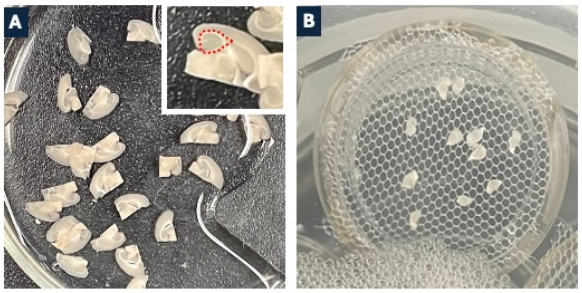

Figure 4. Dissection and placement of hippocampal slices for extracellular field recordings.
(A) Transverse 400 µm hemibrain slices collected in a chilled petri dish. Inset: schematic highlighting the region of the hemibrain slice where the hippocampal formation is dissected away from surrounding neocortex and subcortical structures, indicated with a dotted red line. (B) Isolated hippocampal slices positioned on a mesh support within an interface recording chamber. Continuous perfusion with carbogenated ACSF provides oxygenation and nutrient exchange, maintaining slice viability during extracellular field potential recordings.

physiological levels (2–2.5 mM) while magnesium is lowered to ~1 mM. Higher Ca^{2+} in ACSF is necessary for normal neurotransmitter release and postsynaptic signaling, ensuring that synaptic transmission measured during experiments reflects in vivo conditions.

The final step of recovery occurs when slices are transferred to the recording chamber warmed to 30–32 °C, where they are superfused with carbogenated ACSF (Figure 5). This gradual warming from ice-cold cutting conditions to near-physiological temperature is essential, as it allows slices to adapt to increased metabolic demands without inducing thermal stress. At this temperature range, enzymatic reactions, channel kinetics, and synaptic vesicle release nearly similar to in vivo physiology, producing stable and reproducible field potentials. Some laboratories employ interface chambers, which maximize oxygenation by exposing slices to humidified carbogen above the ACSF, whereas others use submersion chambers, where slices are continuously bathed in flowing ACSF. Both approaches have advantages; interface chambers favor robust LTP, while submerged chambers facilitate whole-cell patch recordings. In some experiments, the CA3 region is surgically removed after recovery to prevent recurrent excitatory activity from reverberating back into CA1, thereby isolating Schaffer collateral input (Madison and Nicoll, 1984). This step is particularly useful when field recordings are used to quantify long-term potentiation, as it eliminates polysynaptic contamination and ensures that evoked responses

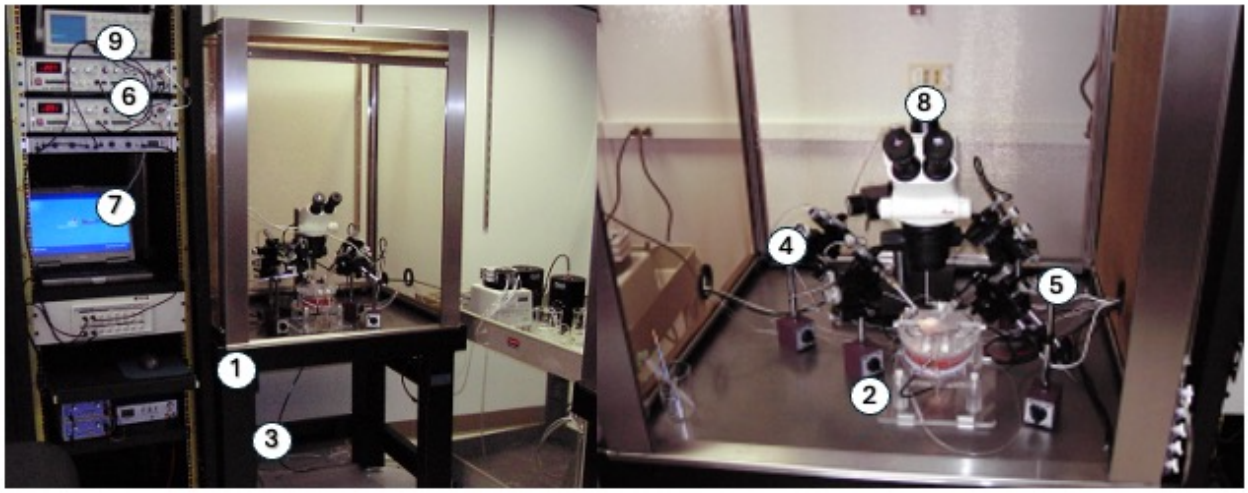

Figure 5. Extracellular field-recording rig (interface slice chamber).
Representative electrophysiology workstation for field recordings from acute brain slices in an interface chamber. The setup comprises: (1) a vibration-isolation table with an acoustic/Faraday enclosure to reduce mechanical and electrical noise; (2) an interface slice chamber (humidified, warmed) with continuous perfusion of carbogenated ACSF delivered from a reservoir via peristaltic pump, in-line bubble trap, flow meter, and in-line heater/thermistor feedback with temperature controller; (3) a stimulating electrode (e.g., bipolar Pt/Ir or tungsten) driven by a constant-current stimulus isolator receiving TTL commands from the acquisition computer; (4) a recording electrode (pulled glass micropipette, ~1–3 MΩ) mounted on a low-drift micromanipulator for positioning in the target layer (e.g., CA1 stratum radiatum) to measure extracellular fEPSPs/population spikes; (5) a headstage and differential extracellular amplifier with selectable gain and hardware filters (high-pass/low-pass), followed by a digitizer (A/D converter) connected to the control PC; (6) control and acquisition software on the computer for protocol design (input–output curves, paired-pulse, LTP/LTD), stimulus timing, and real-time display/analysis; (7) an upright microscope with low-power optics (and optional camera/IR-DIC) for slice visualization; (8) a grounding bus and shielded BNC cabling to minimize 50/60-Hz interference; (9) auxiliary devices including a gas mixer (95% O_2/5% CO_2) for ACSF oxygenation, solution pre-heater, waste collection, and power conditioning/UPS. Together, these components permit stable, low-noise extracellular recordings in interface conditions while delivering precise electrical stimulation and tightly controlled temperature, oxygenation, and flow.

represent monosynaptic CA3-CA1 transmission. This method is used, but it is not necessary for Schaefer collateral synapse recording.

Recording Setup

Slices are transferred to the recording chamber, where temperature is maintained at 30–32 °C for most field recordings or at room temperature for certain whole-cell protocols. A bipolar stimulating electrode (platinum–iridium or tungsten) is positioned in the Schaffer collateral pathway, and a glass microelectrode (1–3 MΩ) filled with ACSF is placed in the stratum radiatum of CA1 to record synaptic responses (Andersen et al., 1971; Manabe et al., 1993). Field excitatory postsynaptic potentials (fEPSPs) are evoked with test pulses delivered at 0.05 Hz, a low frequency chosen to avoid induction of synaptic plasticity during baseline acquisition (Malenka and Bear, 2004). Only slices that exhibit stable baselines, defined as less than 5% drift in fEPSP slope over a 20-minute monitoring period, are included for further analysis.

Stable baselines are essential because they ensure that subsequent changes in synaptic responses reflect genuine, stimulation-induced plasticity rather than spontaneous fluctuations in slice health or recording conditions. An unstable baseline may indicate poor slice viability, incomplete recovery of neuronal excitability, mechanical drift of the electrode, or deterioration of synaptic connections. If baseline responses are drifting upward, it could suggest pre-potentiation or spontaneous network activity that contaminates the true induction effect. Conversely, downward drift may reflect slice deterioration or loss of viable synapses. In either case, including unstable baselines would compromise the interpretation of input–output curves, paired-pulse analyses, and especially LTP experiments, where the key outcome measure is a relative increase in fEPSP slope compared to baseline. By enforcing stringent stability criteria, experimenters can confidently attribute post-stimulation changes to physiological mechanisms of plasticity rather than experimental artifacts.

Often there are challenges with maintaining a stable baseline prior to delivery of high-frequency stimulation. If fEPSP baselines drift more than 5%, several factors should be checked. First, ensure that the slice has had sufficient recovery time. Slices tested

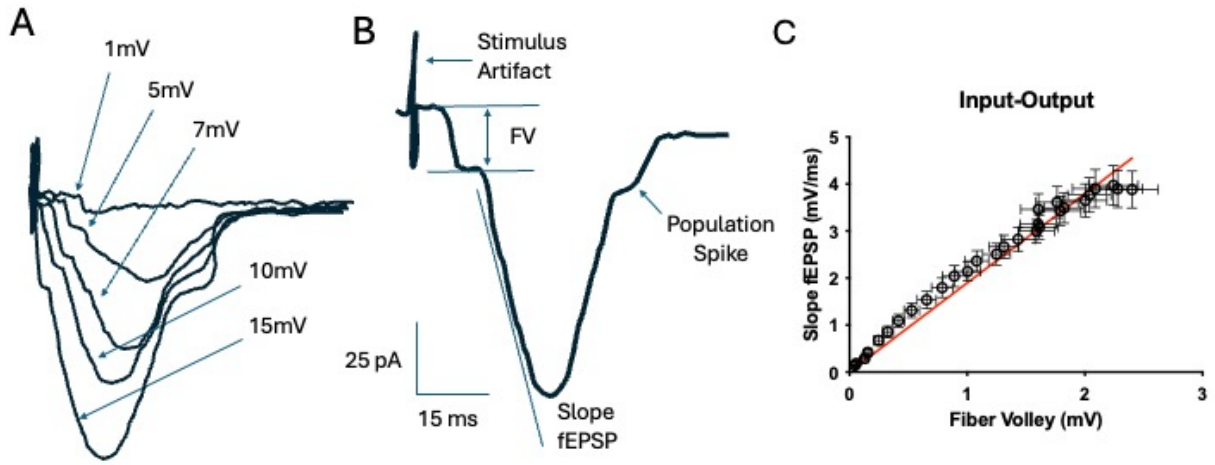

Figure 6. Theoretical input-output analysis of Schaffer collateral-CA1 synaptic responses.
(A) Example traces of field excitatory postsynaptic potentials (fEPSPs) recorded in stratum radiatum of CA1 with increasing stimulation intensities, ranging from 1 mV to 15 mV. As stimulus strength increases, both the presynaptic fiber volley and postsynaptic fEPSP slope increase in a graded manner. (B) Schematic of an individual fEPSP illustrating how the presynaptic fiber volley (initial negative deflection reflecting axonal activation) and the postsynaptic response (initial slope of the fEPSP) are measured. The fiber volley amplitude is used as an index of the number of activated presynaptic axons, while the fEPSP slope reflects the postsynaptic synaptic response. (C) Input–output curve constructed by plotting fiber volley amplitude (x-axis) against fEPSP slope (y-axis). This relationship provides a quantitative measure of synaptic gain and is commonly used to assess basal synaptic transmission, compare pre- and postsynaptic contributions, and select an appropriate stimulus intensity (typically 35–50% of maximal response) for subsequent paired-pulse and long-term potentiation experiments.

too soon after cutting often display unstable excitability. Second, confirm electrode stability: mechanical drift from vibration, perfusion turbulence, or loose micromanipulator clamping can cause artificial slope shifts. Third, evaluate perfusion flow rate and oxygenation; poor ACSF circulation or inadequate carbogenation can compromise slice viability over time. Finally, assess slice quality: pale or edematous slices are more likely to deteriorate during recording and should be excluded. Addressing these factors is critical for maintaining the fidelity of baseline recordings and ensuring reliable measures of synaptic plasticity.

Input-Output Curves

Synaptic gain is quantified by constructing input–output (I/O) curves. Stimulation intensity is systematically varied (typically 2.5–45 µA), and the slope of the fEPSP is plotted against either the applied current or the amplitude of the presynaptic fiber volley. Six sweeps per intensity are averaged to reduce variability, and the test intensity used for subsequent experiments is selected to evoke ~35–50% of the maximal fEPSP slope. This operating point ensures that responses are positioned within the dynamic range for detecting potentiation without risking ceiling effects or saturating the synapse.

The rationale for performing I/O curves is twofold. First, they provide a functional measure of basal synaptic strength as the relationship between stimulus intensity and postsynaptic response amplitude reflects how efficiently presynaptic activity is translated into postsynaptic depolarization. A rightward shift in the curve (requiring more current for the same fEPSP slope) may indicate reduced postsynaptic sensitivity, altered receptor density, or impaired excitatory drive. Conversely, an increased slope at lower intensities can suggest enhanced postsynaptic responsiveness or synaptic hyperexcitability. Second, I/O curves allow investigators to infer aspects of presynaptic function by correlating the presynaptic fiber volley amplitude (reflecting the number of activated axons) with the postsynaptic response. A reduced postsynaptic response for a given fiber volley may reflect decreased neurotransmitter release probability, impaired vesicle cycling, or postsynaptic receptor dysfunction. In contrast, a strong linear relationship between volley size and fEPSP slope suggests intact coupling between presynaptic activation, causing neurotransmitter release, and postsynaptic responsiveness. Thus, constructing I/O curves is not only a technical step for choosing an appropriate test stimulus, but it is also an essential analytic tool for detecting subtle pre- and

postsynaptic alterations in animal models of human neurological disorders.

LTP Induction Paradigms

Long-term potentiation (LTP) is induced in a threshold, nonlinear manner: weak activity yields only short-term potentiation, whereas sufficiently strong, patterned synaptic activity produces stable LTP. High-frequency stimulation (HFS) protocols are therefore used both to probe the induction threshold and, by escalating stimulus strength, to test the maximum capacity of the plasticity machinery of neurons. In hippocampal CA1, a common starting point is to set baseline test pulses at an intensity that evokes ~30–40% of the maximal fEPSP slope and then apply brief 100 Hz trains to cross the induction threshold. The 30-40% is used to preserve dynamic range of the fEPSP, avoiding ceiling effects and population spikes so that subsequent potentiation can be detected as a proportional increase in initial slope rather than saturating the input–output relation.

A widely used, "classical" HFS protocol consists of two 1 second trains at 100 Hz separated by approximately 20 seconds. In mouse CA1, this produces robust LTP that is largely extracellular signal-regulated kinase-(ERK) independent; whereas in rat CA1, the same pattern is ERK-dependent, representing an instructive species difference when interpreting signaling requirements (English and Sweatt, 1997; Selcher et al., 2002). Increasing HFS strength can be done either by adding trains or, more effectively, by spacing trains by minutes (e.g., 4×1-second 100 Hz trains, 5–10 minutes apart) to recruit cAMP/PKA-CREB signaling and protein synthesis associated with late-phase LTP (Huang and Kandel, 1994; Frey and Morris, 1997). Pattern also matters: theta-patterned paradigms, either continuous theta-frequency stimulation (~5 Hz for ~30 seconds) or theta-burst stimulation (TBS; bursts of 4 pulses at 100 Hz repeated at 5 Hz, often delivered in two to three short trains), tend to impose a stronger requirement for ERK signaling in mouse CA1 than the massed 100 Hz protocol, despite comparable pulse counts (English and Sweatt, 1997; Selcher et al., 2002).

For mechanistic dissection, our laboratory also employs "ultra-high-frequency" stimulation (uHFS; e.g., 200 Hz for 1 second, repeated three times at approximately 4-minute intervals), which can elicit LTP that is comparatively NMDA receptor–independent and more reliant on voltage-gated Ca^{2+} entry. This allows investigators to separate defects in NMDAR-gated induction from downstream expression machinery; if a preparation fails to potentiate with NMDAR-dependent HFS/TBS but responds normally to uHFS, the defect likely lies in the induction route rather than the capacity for AMPAR insertion and synaptic strengthening (Weeber et al., 2003). Critically, saturating stimulation by escalating

Paradigm	Pattern & Parameters	Mechanistic Emphasis	Species Note	Typical Use
Classical HFS	2 × 1-sec trains @ 100 Hz, 20 sec apart	NMDAR-dependent induction; postsynaptic expression	Mouse CA1 largely ERK-independent; rat CA1 ERK-dependent	Standard LTP induction and cross-species comparison
Spaced HFS (late-LTP bias)	4 × 1-sec trains @ 100 Hz, 5–10 min apart	Recruits cAMP/PKA-CREB and protein synthesis (late LTP)	As above	Tests consolidation /translation dependence
Theta-frequency stimulation (TFS)	~5 Hz continuous for ~30 sec	Stronger ERK requirement in mouse CA1	ERK-sensitive	Naturalistic pattern; tests induction pathway dependence
Theta-burst stimulation (TBS)	Bursts of 4 pulses @ 100 Hz, repeated at 5 Hz; 2–3 short trains	NMDAR-dependent; ERK-sensitive in mouse CA1	ERK-sensitive	Mimics theta-modulated bursts; efficient induction at lower total pulses
Ultra-high-frequency stimulation (uHFS)	1-sec @ 200 Hz, repeated 3 × at ~4-min intervals	Comparatively NMDA-independent; relies more on voltage-gated Ca^{2+} entry	—	Dissects induction route vs expression capacity; useful when NMDAR-dependent LTP fails

threshold-level HFS/TBS to spaced, repeated induction until additional bouts produce no further increase in fEPSP slope provides an operational readout of the network's maximum LTP capacity. This is especially informative in models with suspected plasticity deficits (e.g., Angelman syndrome, Fragile X models, or Reelin deficiency (Weeber et al., 2003; Beffert et al., 2005; Yau et al., 2016). If threshold-level protocols are impaired but saturating stimulation achieves near-wild-type potentiation, the core capacity is intact and the phenotype reflects an elevated induction threshold or altered excitability. Conversely, if potentiation remains subnormal even after saturating HFS, the ceiling itself is reduced, implicating limits in expression or metaplastic state. In practice, investigators often combine these paradigms within the same slice (with independent input pathways to verify input specificity) to map the full stimulus–response surface of LTP from threshold to ceiling.

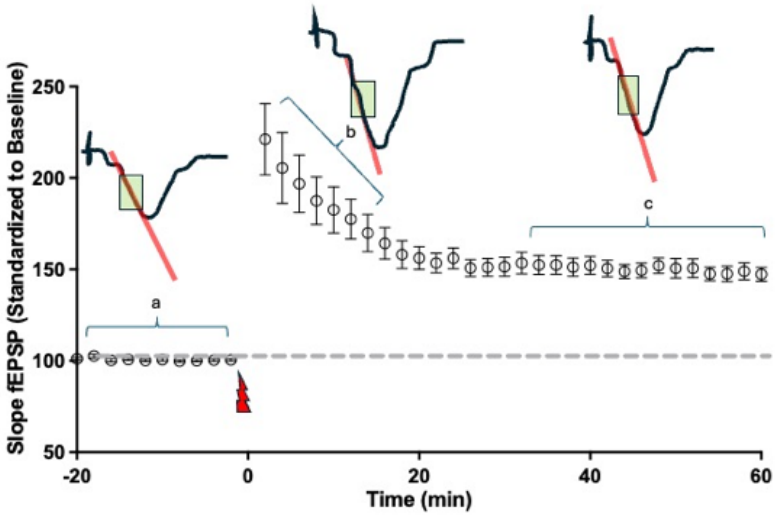

Figure 7. Example LTP experiment in hippocampal CA1.
A 20-min baseline was recorded with low-frequency test pulses, followed by delivery of high-frequency stimulation (HFS; indicated by the lightning bolt icon), and responses were monitored for 60 min post-HFS. (a) Representative baseline fEPSP; the light green box marks the fixed analysis window on the rising phase (after the fiber volley and before any population spike), and the red line indicates the linear fit used to compute the initial slope. (b) Representative fEPSP collected immediately after HFS (early post-induction), with the same analysis window and slope fit shown. (c) Representative fEPSP collected 40–60 min post-HFS (late phase), with identical window placement and slope fit. For quantification (not shown), fEPSP slopes are normalized to the mean baseline and expressed as percent of baseline; identical filtering and windowing are used across all panels. Scale bars as indicated; analysis window and slope fit are identical across a–c.

Data Acquisition and Analysis

Field EPSPs are acquired from CA1 stratum radiatum with test pulses set to evoke ~30–40% of the maximal fEPSP to avoid population spikes, digitized at 10 kHz and hardware– or software–low-pass filtered at 2 kHz (no additional smoothing), then quantified by the initial slope measured on the linear rising phase. To ensure physiological relevance and comparability, the slope is calculated with a fixed, pre-registered window positioned after the fiber volley and before any population spike. For example, a 1–2 millisecond window anchored to the end of the fiber volley or the segment spanning ~10–40% of the waveform's peak using linear regression (not peak amplitude) so that small differences in kinetics do not distort the metric. The exact placement of this window must remain identical across baseline and post-induction epochs, animals, and groups; changing the window or filter settings mid-experiment can create artifactual "plasticity." Responses are normalized to the mean baseline slope (typically the last 10–15 minutes before induction) and expressed as the percent of baseline; LTP magnitude is reported as the average potentiation over 45–60 minutes after induction, or a prespecified late window that can last up to 3 hours post tetanus (Malenka and Bear, 2004; Whitlock et al., 2006). Data quality controls are essential: maintain high SNR, stable electrode placement and stimulus intensity, and avoid over-filtering (which can blunt the rising phase and underestimate slope). Exclude datasets with unstable baselines (e.g., >5% drift or rising noise floor), movement or electrical artifacts, spontaneous or stimulus-evoked population spikes contaminating the slope window, or large fiber-volley jitter. Adhering to these acquisition and analysis conventions that require clean, minimally filtered traces, fixed, well-defined slope window, and strict stability criteria will yield robust, reproducible fEPSP measurements sensitive to true changes in synaptic strength.

Paired-Pulse Facilitation in Acute Hippocampal Slices

Paired-pulse facilitation (PPF) is a classic electrophysiological technique used to assess presynaptic function by measuring short-term plasticity of synaptic transmission. When two stimuli are delivered in rapid succession to a presynaptic input, the second postsynaptic response is typically enhanced relative to the first. This facilitation is attributed to residual calcium remaining in presynaptic terminals following the first stimulus, which increases the probability of neurotransmitter vesicle release during the second (Zucker and Regehr, 2002). Importantly, PPF provides insight into presynaptic release probability, complementing information obtained from input–output (I/O) experiments. While I/O curves characterize postsynaptic responsiveness to varying stimulus strengths, PPF directly probes the dynamics of neurotransmitter release. Combining these approaches enables investigators to parse presynaptic versus postsynaptic contributions to synaptic function, thereby producing a more complete understanding of circuit physiology. For example, a slice showing a steep I/O relationship but reduced PPF may indicate high postsynaptic sensitivity coupled with high presynaptic release probability, whereas the opposite pattern may suggest reduced release probability as a limiting factor.

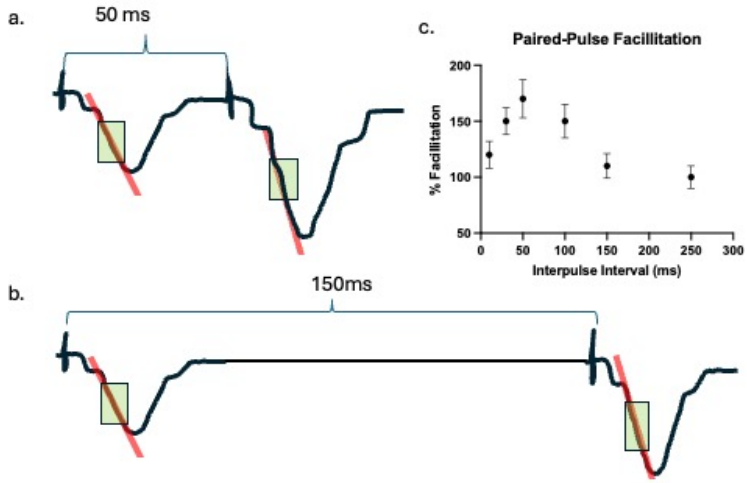

Figure 8. Paired-pulse facilitation (PPF) at Schaffer collateral-CA1 synapses.
(a) Representative field excitatory postsynaptic potentials (fEPSPs) evoked by two stimuli delivered at a 30 ms interpulse interval (IPI). The second fEPSP exhibits a steeper initial slope compared to the first (green box highlights the slope measurement region; red line indicates slope calculation).
(b) Representative fEPSPs recorded with a 150 ms IPI, showing a reduced facilitation of the second response relative to the first.
(c) Summary input–output graph of theoretical paired-pulse ratios (PPR, $slope_2/slope_1 \times 100\%$) across multiple IPIs (10, 30, 50, 100, and 150 ms). The curve illustrates the expected decay of facilitation as the IPI increases, reflecting presynaptic release probability and short-term synaptic dynamics in CA1 hippocampal circuits.

To elicit PPF, two identical stimuli are delivered at a fixed intensity, commonly set to evoke 30–40% of the maximal fEPSP slope. Interpulse intervals ranging from 20–250 milliseconds are applied, with shorter intervals (20–50 ms) producing more pronounced facilitation due to greater residual calcium accumulation. The paired-pulse ratio (PPR) is calculated by dividing the slope of the second fEPSP by the slope of the first. Repeating this procedure across several interpulse intervals generates a facilitation curve that reflects synaptic release probability.

By incorporating I/O curves into the same experimental paradigm, researchers can better contextualize PPF findings. For instance, if I/O experiments reveal altered postsynaptic responsiveness but PPF ratios remain unchanged, the underlying deficit is more likely postsynaptic. Conversely, changes in both I/O slopes and PPF may indicate combined presynaptic and postsynaptic dysfunction. This dual assessment strengthens the interpretive power of hippocampal field recordings and provides a robust framework for dissecting the mechanisms underlying synaptic transmission and plasticity. Paired-pulse facilitation (PPF) is a short-term form of synaptic plasticity that reflects presynaptic release probability.

Discussion

The maternal Ube3a null mouse ($Ube3a^{m-/p+}$), first reported by Jiang et al. (1998), has consistently shown impaired hippocampus-dependent learning accompanied by blunted CA1 LTP, cementing SC-CA1 synapses as a core electrophysiological readout of the disorder (Jiang et al., 1998; Miura et al., 2002; Jiang et al., 2010; Silva-Santos et al., 2015; Judson et al., 2016; Dodge et al., 2020; Lee et al., 2023). Importantly, mechanistic work has linked LTP deficits

to altered calcium/calmodulin-dependent protein kinase II (CaMKII) signaling: Ube3a loss impairs experience-dependent autophosphorylation of CaMKII at threonine-286, which is required for stable synaptic potentiation (Weeber et al., 2003; van Woerden et al., 2007). This disrupted coupling between N-methyl-D-aspartate receptor (NMDAR) activation and downstream kinase signaling suggests that UBE3A deficiency primarily raises the threshold for LTP induction, rendering weak or moderate stimulation insufficient to trigger long-lasting potentiation. However, in some experimental contexts, more robust induction protocols such as multiple trains of 100 Hz HFS or pharmacological disinhibition with GABA receptor antagonists (Cecere et al., 2025) can restore LTP toward wild-type levels. These findings imply that the fundamental capacity for synaptic strengthening remains intact, but access to that capacity is limited by heightened inhibitory tone or impaired NMDAR–CaMKII coupling. By contrast, other studies demonstrate that even saturating LTP protocols fail to normalize potentiation, indicating that downstream expression mechanisms, such as AMPA receptor trafficking, actin cytoskeletal remodeling, or mTORC1-dependent translational regulation, may be intrinsically disrupted (Sun et al., 2016).

Saturating long-term potentiation (LTP) paradigms provide critical insight into the distinction between synaptic induction threshold and maximum plasticity capacity in hippocampal CA1 circuits. By progressively escalating stimulation intensity, via multiple trains of high-frequency stimulation (HFS) at 100 Hz or repeated theta-burst stimulation (TBS), investigators can drive the system toward a saturation point, beyond which additional stimulation produces minimal further increases in the field excitatory postsynaptic potential (fEPSP) slope, typically plateauing at a 5–10% gain. Studies in Ube3a maternal-null (m−/p+) mice have revealed two distinct patterns. In some cases, weak or near-threshold protocols fail to induce stable potentiation, or the potentiation decays rapidly, yet robust plasticity can still be achieved with stronger or pharmacologically facilitated stimulation. This suggests that Ube3a deficiency primarily elevates the induction threshold rather than constraining the ultimate capacity for LTP. Such findings are consistent with reports of reduced NMDA receptor function, impaired NMDAR–CaMKII coupling and altered inhibitory tone in AS models (Miura et al., 2002; Weeber et al., 2003; Judson et al., 2016).

Conversely, other studies have demonstrated that even under saturating HFS or repeated TBS, the maximum potentiation achieved in Ube3a-deficient mice remains below wild-type levels. This “true ceiling” effect points toward deficits in expression or maintenance mechanisms, such as impaired AMPA receptor trafficking, actin cytoskeletal remodeling, or dysregulated translational control pathways like mTORC1, which can be corrected only through direct molecular interventions such as Ube3a reinstatement or pathway modulation (Silva-Santos et al., 2015; Lee et al., 2023). However, LTP magnitude is strongly influenced by experimental parameters, including slice preparation, recording temperature, and stimulus intensity (as described above). Variability in fiber volley recruitment across preparations can obscure whether differences reflect a genuine reduction in the maximum expression capacity of synaptic potentiation or simply reduced input–output coupling under specific conditions. Without rigorous normalization to presynaptic drive (e.g., fiber volley amplitude) and control for slice health, apparent “ceiling” differences may instead represent threshold-related impairments in induction. Furthermore, the canonical LTP paradigms used, such as saturating 100 Hz HFS or multiple-train TBS, rely heavily on NMDA receptor activation and CaMKII autophosphorylation, and reduced LTP in these contexts may not unequivocally indicate an intrinsic limit in plasticity expression capacity, but rather reflect an impaired ability to engage induction mechanisms.

Beyond revealing the parameters of induction and ceiling, saturating LTP experiments in AS mouse and rat models have provided a framework for dissecting the mechanistic underpinnings of synaptic dysfunction. Evidence from the Ube3a deletion rat model indicates comparable deficits in hippocampal plasticity, reinforcing the cross-species validity of the threshold-versus-capacity framework (Berg et al., 2020; Dodge et al., 2020). Together, these findings demonstrate that using multiple LTP paradigms can move beyond simply confirming impaired plasticity to provide a mechanistic resolution, distinguishing between deficits in induction versus expression. This mechanistic insight is essential for guiding therapeutic

strategies for AS. In particular, interventions that enhance excitatory drive or reduce inhibition may overcome elevated thresholds, while approaches targeting translational or structural pathways, or reactivating the paternal allele, may be necessary to restore the full capacity for long-term synaptic strengthening.

Acknowledgements

The authors wish to thank Dr. Kelly Knee for editing and insight.

References

Aghajanian GK, Sprouse JS, Sheldon P, Rasmussen K (1990) Electrophysiology of the central serotonin system: receptor subtypes and transducer mechanisms. Ann N Y Acad Sci 600:93-103; discussion 103.

Amaral DG, Scharfman HE, Lavenex P (2007) The dentate gyrus: fundamental neuroanatomical organization (dentate gyrus for dummies). Prog Brain Res 163:3-22.

Beffert U, Durudas A, Weeber EJ, Stolt PC, Giehl KM, Sweatt JD, Hammer RE, Herz J (2006) Functional dissection of Reelin signaling by site-directed disruption of Disabled-1 adaptor binding to apolipoprotein E receptor 2: distinct roles in development and synaptic plasticity. J Neurosci 26:2041-2052.

Beffert U, Weeber EJ, Durudas A, Qiu S, Masiulis I, Sweatt JD, Li WP, Adelmann G, Frotscher M, Hammer RE, Herz J (2005) Modulation of synaptic plasticity and memory by Reelin involves differential splicing of the lipoprotein receptor Apoer2. Neuron 47:567-579.

Berg EL et al. (2020) Translational outcomes in a full gene deletion of ubiquitin protein ligase E3A rat model of Angelman syndrome. Transl Psychiatry 10:39.

Bi GQ, Poo MM (1998) Synaptic modifications in cultured hippocampal neurons: dependence on spike timing, synaptic strength, and postsynaptic cell type. J Neurosci 18:10464-10472.

Bliss TV, Lomo T (1973) Long-lasting potentiation of synaptic transmission in the dentate area of the anaesthetized rabbit following stimulation of the perforant path. J Physiol 232:331-356.

Bliss TV, Richter-Levin G (1993) Spatial learning and the saturation of long-term potentiation. Hippocampus 3:123-125.

Bliss TV, Collingridge GL (1993) A synaptic model of memory: long-term potentiation in the hippocampus. Nature 361:31-39.

Cecere G et al. (2025) Preclinical pharmacology of alogabat: a novel GABA(A)-alpha5 positive allosteric modulator targeting neurodevelopmental disorders with impaired GABA(A) signaling. Front Pharmacol 16:1626078.

Collingridge GL, Kehl SJ, McLennan H (1983) Excitatory amino acids in synaptic transmission in the Schaffer collateral-commissural pathway of the rat hippocampus. J Physiol 334:33-46.

Dodge A, Peters MM, Greene HE, Dietrick C, Botelho R, Chung D, Willman J, Nenninger AW, Ciarlone S, Kamath SG, Houdek P, Sumova A, Anderson AE, Dindot SV, Berg EL, O'Geen H, Segal DJ, Silverman JL, Weeber EJ, Nash KR (2020) Generation of a Novel Rat Model of Angelman Syndrome with a Complete Ube3a Gene Deletion. Autism Res 13:397-409.

Eccles JC (1979) Hippocampal plasticity. Prog Brain Res 51:133-138.

Eichenbaum H (2017) The role of the hippocampus in navigation is memory. J Neurophysiol 117:1785-1796.

English JD, Sweatt JD (1997) A requirement for the mitogen-activated protein kinase cascade in hippocampal long term potentiation. J Biol Chem 272:19103-19106.

Frey U, Morris RG (1997) Synaptic tagging and long-term potentiation. Nature 385:533-536.

Hajos N, Mody I (2009) Establishing a physiological environment for visualized in vitro brain slice recordings by increasing oxygen supply and modifying aCSF content. J Neurosci Methods 183:107-113.

Huang YY, Kandel ER (1994) Recruitment of long-lasting and protein kinase A-dependent long-term potentiation in the CA1 region of hippocampus requires repeated tetanization. Learn Mem 1:74-82.

Jiang YH, Armstrong D, Albrecht U, Atkins CM, Noebels JL, Eichele G, Sweatt JD, Beaudet AL (1998) Mutation of the Angelman ubiquitin ligase in mice causes increased cytoplasmic p53

and deficits of contextual learning and long-term potentiation. Neuron 21:799-811.

Jiang YH, Pan Y, Zhu L, Landa L, Yoo J, Spencer C, Lorenzo I, Brilliant M, Noebels J, Beaudet AL (2010) Altered ultrasonic vocalization and impaired learning and memory in Angelman syndrome mouse model with a large maternal deletion from Ube3a to Gabrb3. PLoS One 5:e12278.

Judson MC, Wallace ML, Sidorov MS, Burette AC, Gu B, van Woerden GM, King IF, Han JE, Zylka MJ, Elgersma Y, Weinberg RJ, Philpot BD (2016) GABAergic Neuron-Specific Loss of Ube3a Causes Angelman Syndrome-Like EEG Abnormalities and Enhances Seizure Susceptibility. Neuron 90:56-69.

Kandel ER (2001) The molecular biology of memory storage: a dialog between genes and synapses. Biosci Rep 21:565-611.

Lee D, Chen W, Kaku HN, Zhuo X, Chao ES, Soriano A, Kuncheria A, Flores S, Kim JH, Rivera A, Rigo F, Jafar-Nejad P, Beaudet AL, Caudill MS, Xue M (2023) Antisense oligonucleotide therapy rescues disturbed brain rhythms and sleep in juvenile and adult mouse models of Angelman syndrome. Elife 12.

Levenson J, Weeber E, Selcher JC, Kategaya LS, Sweatt JD, Eskin A (2002) Long-term potentiation and contextual fear conditioning increase neuronal glutamate uptake. Nat Neurosci 5:155-161.

Lisman J, Schulman H, Cline H (2002) The molecular basis of CaMKII function in synaptic and behavioural memory. Nat Rev Neurosci 3:175-190.

Maclver MB, Mikulec AA, Amagasu SM, Monroe FA (1996) Volatile anesthetics depress glutamate transmission via presynaptic actions. Anesthesiology 85:823-834.

Madison DV, Nicoll RA (1984) Control of the repetitive discharge of rat CA 1 pyramidal neurones in vitro. J Physiol 354:319-331.

Malenka RC, Bear MF (2004) LTP and LTD: an embarrassment of riches. Neuron 44:5-21.

Malinow R, Malenka RC (2002) AMPA receptor trafficking and synaptic plasticity. Annu Rev Neurosci 25:103-126.

Manabe T, Wyllie DJ, Perkel DJ, Nicoll RA (1993) Modulation of synaptic transmission and long-term potentiation: effects on paired pulse facilitation and EPSC variance in the CA1 region of the hippocampus. J Neurophysiol 70:1451-1459.

Megias M, Emri Z, Freund TF, Gulyas AI (2001) Total number and distribution of inhibitory and excitatory synapses on hippocampal CA1 pyramidal cells. Neuroscience 102:527-540.

Miura K, Kishino T, Li E, Webber H, Dikkes P, Holmes GL, Wagstaff J (2002) Neurobehavioral and electroencephalographic abnormalities in Ube3a maternal-deficient mice. Neurobiol Dis 9:149-159.

Moretti P, Levenson JM, Battaglia F, Atkinson R, Teague R, Antalffy B, Armstrong D, Arancio O, Sweatt JD, Zoghbi HY (2006) Learning and memory and synaptic plasticity are impaired in a mouse model of Rett syndrome. J Neurosci 26:319-327.

O'Keefe J, Dostrovsky J (1971) The hippocampus as a spatial map. Preliminary evidence from unit activity in the freely-moving rat. Brain Res 34:171-175.

Palop JJ, Mucke L, Roberson ED (2011) Quantifying biomarkers of cognitive dysfunction and neuronal network hyperexcitability in mouse models of Alzheimer's disease: depletion of calcium-dependent proteins and inhibitory hippocampal remodeling. Methods Mol Biol 670:245-262.

Payne K, Wilson CJ, Young S, Fifkova E, Groves PM (1982) Evoked potentials and long-term potentiation in the mouse dentate gyrus after stimulation of the entorhinal cortex. Exp Neurol 75:134-148.

Remondes M, Schuman EM (2002) Direct cortical input modulates plasticity and spiking in CA1 pyramidal neurons. Nature 416:736-740.

Schwartzkroin PA, Wester K (1975) Long-lasting facilitation of a synaptic potential following tetanization in the in vitro hippocampal slice. Brain Res 89:107-119.

Selcher JC, Weeber EJ, Varga AW, Sweatt JD, Swank M (2002) Protein kinase signal transduction cascades in mammalian associative conditioning. Neuroscientist 8:122-131.

Silva-Santos S, van Woerden GM, Bruinsma

CF, Mientjes E, Jolfaei MA, Distel B, Kushner SA, Elgersma Y (2015) Ube3a reinstatement identifies distinct developmental windows in a murine Angelman syndrome model. J Clin Invest 125:2069-2076.

Snyder GL, Galdi S, Hendrick JP, Hemmings HC, Jr. (2007) General anesthetics selectively modulate glutamatergic and dopaminergic signaling via site-specific phosphorylation in vivo. Neuropharmacology 53:619-630.

Speigel I, Patel K, Osman V, Hemmings HC, Jr. (2023) Volatile anesthetics inhibit presynaptic cGMP signaling to depress presynaptic excitability in rat hippocampal neurons. Neuropharmacology 240:109705.

Spruston N (2008) Pyramidal neurons: dendritic structure and synaptic integration. Nat Rev Neurosci 9:206-221.

Sun J, Liu Y, Tran J, O'Neal P, Baudry M, Bi X (2016) mTORC1-S6K1 inhibition or mTORC2 activation improves hippocampal synaptic plasticity and learning in Angelman syndrome mice. Cell Mol Life Sci 73:4303-4314.

Sweatt JD (2004) Mitogen-activated protein kinases in synaptic plasticity and memory. Curr Opin Neurobiol 14:311-317.

Ting JT, Daigle TL, Chen Q, Feng G (2014) Acute brain slice methods for adult and aging animals: application of targeted patch clamp analysis and optogenetics. Methods Mol Biol 1183:221-242.

van Woerden GM, Harris KD, Hojjati MR, Gustin RM, Qiu S, de Avila Freire R, Jiang YH, Elgersma Y, Weeber EJ (2007) Rescue of neurological deficits in a mouse model for Angelman syndrome by reduction of alphaCaMKII inhibitory phosphorylation. Nat Neurosci 10:280-282.

Viana Di Prisco G (1984) Hebb synaptic plasticity. Prog Neurobiol 22:89-102.

Weeber EJ, Jiang YH, Elgersma Y, Varga AW, Carrasquillo Y, Brown SE, Christian JM, Mirnikjoo B, Silva A, Beaudet AL, Sweatt JD (2003) Derangements of hippocampal calcium/calmodulin-dependent protein kinase II in a mouse model for Angelman mental retardation syndrome. J Neurosci 23:2634-2644.

Whitlock JR, Heynen AJ, Shuler MG, Bear MF (2006) Learning induces long-term potentiation in the hippocampus. Science 313:1093-1097.

Witter MP (2007) Intrinsic and extrinsic wiring of CA3: indications for connectional heterogeneity. Learn Mem 14:705-713.

Yau SY, Bostrom CA, Chiu J, Fontaine CJ, Sawchuk S, Meconi A, Wortman RC, Truesdell E, Truesdell A, Chiu C, Hryciw BN, Eadie BD, Ghilan M, Christie BR (2016) Impaired bidirectional NMDA receptor dependent synaptic plasticity in the dentate gyrus of adult female Fmr1 heterozygous knockout mice. Neurobiol Dis 96:261-270.

Zalutsky RA, Nicoll RA (1990) Comparison of t wo forms of long-term potentiation in single hippocampal neurons. Science 248:1619-1624.

Zorumski CF, Izumi Y, Mennerick S (2016) Ketamine: NMDA Receptors and Beyond. J Neurosci 36:11158-11164.

Zucker RS, Regehr WG (2002) Short-term synaptic plasticity. Annu Rev Physiol 64:355-405.

FAST-Data, Analysis, Reviews and Techniques
Volume 2 Issue 2

Publication date: August 1, 2026
Publisher: The Thomas Group. 131 Varick St., New York, NY (212-947-6400)

Disclaimers--The FAST-DART Journal contains preprints, which are research manuscripts that have not yet undergone formal peer review. They may contain inaccuracies, errors, or be in draft form, and therefore, the content may not be finalized. The content should not be considered validated and should not be used to guide clinical practice, health behavior or policy decisions. The views expressed in articles published in this journal are those of the authors and do not necessarily reflect the views of the editors or publisher. The Foundation for Angelman Syndrome Therapeutics does not endorse the content, nor does it validate the methods, assumptions, conclusions, or scientific quality presented by the authors. FAST is not responsible for any errors or omissions within the articles. FAST is not liable for any damages resulting from the use or misuse of content within this journal.

Copyright Notice and Licensing—All articles in the Foundation for Angelman Syndrome Therapeutics-Data Analysis Review and Techniques Journal ("FAST-DART Journal") are published under a Creative Commons Attribution License, unless otherwise stated. Redistribution, reuse, or citation of individual articles should follow the license terms listed in each article. Authors retain copyright and grant the journal the right of first publication. Unauthorized use may violate copyright law.

Bioresources for Angelman Syndrome Research

Models, measures, and materials to accelerate Angelman syndrome therapeutic development.

In Vivo Models

(Mouse, rat, pig, fly, DNA icons)

Mouse Model

- AS mouse model (exon 2 deletion) (B6.129S7-Ube3atm1Alb/J)
- AS mouse model on 129 background (129S7-Ube3atm1Alb/J)
- Large deletion AS mouse model *
- Ube3aYFP reporter mouse model
- C57BL/6J-Ube3aem1Alb/MxueJ mouse model
- Additional published mouse models

Rat

- Model Full Ube3a deletion AS rat model *

Pig Model

- AS Pig Model *

Fly Model

- DUbe3a Drosophila
- FVB/N-Tg(tetO-Ube3a*2)884Svd/J and FVB/N-Tg(tetO-Ube3a*1)1Svd/J mouse models
- Additional published overexpression models

In Vitro Models

(Flask or pipette icon)

- Patient-derived induced pluripotent stem cells (iPSCs) for all AS genotypes *
- AS deletion landing pad cell models *
- AS ICD and UPD landing pad cell models *
- Human paternal GFP reporter cell line *
- Human paternal GFP reporter cell line *
- AS organoid models *
- Additional published in vitro models

Kits & Reagants

(tube rack, dropper bottle icon)

- Ubiquitination Assay *
- PHA533533
- Topotecan (Hycamtin)
- Mouse Surrogate ASO

Clinical Endpoints & Biomarkers

(ECG/waveform or bar chart icon)

For the clinical tools like endpoints and biomarkers that are currently being utilized in clinical trials for Angelman syndrome please see the work being done through the Angelman Syndrome Biomarker and Outcome Measure Consortium (A-BOM): https://cureangelman.org/abom

**Developed with FAST support*

Scan the QR code for the full catalog, references, and contacts.

science@cureangelman.org